Diurnal Radiance Patterns of Finite and Semi-Infinite Clouds in Observations of Cloud Fields

by
David M. Ebel
Thomas B. McKee

Department of Atmospheric Science
Colorado State University
Fort Collins, Colorado

Colorado State University

Department of Atmospheric Science

Paper No. 345

DIURNAL RADIANCE PATTERNS OF FINITE AND SEMI-INFINITE CLOUDS IN OBSERVATIONS OF CLOUD FIELDS

by

David M. Ebel

Thomas B. McKee

This research was supported by the
National Science Foundation
under grant ATM78-27556.

Department of Atmospheric Science
Colorado State University
Fort Collins, Colorado
80523

December, 1981

Atmospheric Science Paper No. 345

ABSTRACT

The effects of finite and semi-infinite cloud shape on diurnal satellite observations were investigated by simulating diurnal satellite observations of a finite cubic and semi-infinite cloud and comparing these results with actual diurnal satellite observations of cloud fields. Theoretical satellite observations were created by computing relative radiances from a theoretical model which used the Monte Carlo method to simulate the scattering of solar radiation by a finite and infinite cloud for optical depths of 73.5 and 20.0. The diurnal variations in radiance for an infinite and finite cubic cloud viewed at a zenith angle (θ) of 0° were both symmetric about local noon when the maximum radiance occurred. When viewing the same clouds from an average zenith angle ($\bar{\theta}$) of 18° to 31° (measured westward from zenith), the diurnal variation in radiance for the infinite cloud was again nearly symmetric about local noon when the maximum radiance occurred. The finite cubic cloud, however, had a skewed diurnal variation in radiance with the maximum radiance occurring at 1400 local time. This was true for both optical depths.

The theoretical diurnal variations in radiance for the infinite and finite clouds were then compared to diurnal radiance data from cloud fields observed by geostationary satellite. The comparison was done by forming cumulative distribution functions (CDF) from hourly frequency distributions of digitized visible satellite data. Selected

CDF probability levels were plotted as a function of time and then compared to the theoretical diurnal variation of radiance.

Two cloud fields consisting of cloud clusters that covered more than 90 percent of the 4° latitude by 4° longitude study area were chosen to examine the diurnal radiance pattern of semi-infinite clouds. The observed radiance pattern for both of the observed cloud fields closely resembled the theoretical radiance pattern for an infinite cloud with the pattern being symmetric about local noon when the maximum radiance occurred. This was true for both 4 and 16 n. mi resolution data. Two cloud fields consisting of scattered clouds that covered less than 30 percent of the study areas were chosen to examine the diurnal radiance pattern of finite clouds. The diurnal radiance observations at 4 and 16 n. mi resolutions for both observed cloud fields closely resembled the theoretical radiance pattern for a finite cloud viewed from $\bar{\theta} = 18 \rightarrow 31°$, with the greater radiances occurring during the afternoon hours and peaking at 1400 LT.

The results from the four cloud fields showed that the radiative features of both semi-infinite and finite clouds can be found in satellite observations. This was true not only for the high resolution data (4 n. mi), but also for 16 n. mi resolution data indicating that none of these cloud radiative features were resolution dependent.

ACKNOWLEDGEMENTS

The authors would like to thank Drs. W. Gray and P. Mielke, for their helpful suggestions, Ms. Lee Ann Mitchell and Odilia Panella for their help in typing the manuscript, Mr. John Kleist for his programming assistance and Ms. Judy Sorbie for drafting the figures. This research was supported by the National Science Foundation under grant ATM78-27556. Computer time was provided by the National Center for Atmospheric Research which is supported by the National Science Foundation.

TABLE OF CONTENTS

Chapter		Page
	ABSTRACT	iii
	ACKNOWLEDGEMENTS	v
	LIST OF FIGURES	vii
	LIST OF SYMBOLS	ix
1.	INTRODUCTION	1
	1.1 Background	1
	1.2 Problem and Objectives	2
	1.3 Approach	3
2.	SIMULATED DIURNAL RADIANCE PATTERNS OF A FINITE AND AN INFINITE CLOUD	5
	2.1 Model Description	5
	2.2 Adjustment of Model Radiances to Simulate Satellite Data	11
	2.3 Model Results Simulating Satellite Observations	15
3.	SATELLITE DATA DESCRIPTION AND PROCESSING	23
	3.1 Satellite Characteristics	23
	3.2 Satellite Dataset Description	24
	3.3 Calibration of SMS-1 Visible Satellite Data	25
	3.4 Calibration of SMS-1 Infrared Satellite Data	33
	3.5 Statistical Procedures Performed on Satellite Data	33
4.	DESCRIPTIVE COMPARISON OF SIMULATED DIURNAL SATELLITE OBSERVATIONS WITH SMS-1 DIURNAL SATELLITE DATA	37
	4.1 Comparison of an Infinite Cloud Diurnal Radiance Pattern with Two Selected Cloud Fields	37
	4.1.1 Case 1	37
	4.1.2 Case 2	44
	4.2 Comparison of a Finite Cubic Cloud Diurnal Radiance Pattern with Two Selected Cloud Fields	51
	4.2.1 Case 3	51
	4.2.2 Case 4	56
5.	SUMMARY AND CONCLUSIONS	64
	REFERENCES	67

LIST OF FIGURES

Figure		Page
1	Cumulative probability distribution function for C1 model at $\lambda = 0.7$ μm	9
2	Slab cloud with coordinate system	10
3	Examples of a single satellite observation of a theoretical infinite (a) and finite cubic cloud (b)	13
4	Relative positions of the satellite and a finite cloud situated in the equitorial plane at the equinox	16
5	Theoretical diurnal variation of upwelling radiance as viewed by satellite for an optically thick ($\tau = 73.5$) infinite cloud (top two curves) and finite cubic cloud (bottom two curves) from $\theta = 0°$ (a) and $\theta = 18 \rightarrow 31°$, $\phi = 22°$ (b)	17
6	Same as Figure 5 except $\tau = 20$	20
7	Averaging scheme used to reduce ½ n. mi resolution 6-bit visible data to 2 n. mi resolution 8-bit data	26
8	GATE sector and SMS-1 satellite subpoint (SSP)	27
9	Comparison of NOAA-2 SR (solid line) and SMS-1 VISSR (dashed line) relative response functions	28
10	GATE sector and the four regions of simultaneous measurements by SMS-1 and NOAA-2 on September 17, 1974 near 1000 GMT	30
11	SMS-1 visible photograph from July 8, 1974 containing the Case 1 cloud field	38
12	Diurnal variation of selected CDF probability levels for 4 n. mi resolution IR data for Case 1	40
13	Diurnal variation of selected CDF probability levels for 4 n. mi resolution visible radiances for Case 1	41
14	Diurnal variation of the 50% probability level from Figure 13 and the (90%-60%) difference at 4 and 16 n. mi resolutions for visible radiances	43
15	SMS-1 visible photograph from June 29, 1974 containing the Case 2 cloud field	45
16	Diurnal variation of selected CDF probability levels for 4 n. mi resolution IR data for Case 2	47

LIST OF FIGURES (continued)

Figure		Page
17	Diurnal variation of selected CDF probability levels for 4 n. mi resolution visible radiances for Case 2 . . .	48
18	Diurnal variation of the 50% probability level from Figure 17 and the (90%-60%) difference at 4 and 16 n. mi resolutions for visible radiances	50
19	SMS-1 visible photograph from July 8, 1974 containing the Case 3 cloud field	52
20	Diurnal variation of selected CDF probability levels for 4 n. mi resolution IR data for Case 3	53
21	Diurnal variation of selected CDF probability levels for 4 n. mi resolution visible radiances for Case 3 . . .	55
22	Diurnal variation of the 50% probability level from Figure 21 and the (90%-60%) difference at 4 and 16 n. mi resolutions for visible radiances	57
23	SMS-1 visible photograph from July 13, 1974 containing the Case 4 cloud field	58
24	Diurnal variation of selected CDF probability levels for 4 n. mi resolution IR data for Case 4	60
25	Diurnal variation of selected CDF probability levels for 4 n. mi resolution visible radiances for Case 4 . . .	61
26	Diurnal variation of the 50% probability level from Figure 25 and the (90%-60%) difference at 4 and 16 n. mi resolutions for visible radiances	63

LIST OF SYMBOLS

a	slope
A_T	area of cloud top
A_X	area of X-face of cloud
A_Y	area of Y-face of cloud
b	y-intercept
c_i	6-bit raw count for sensor i
$c_s^{n\ell}$	SMS-1 nonlinear 8-bit raw count
c_s^{ℓ}	SMS-1 linear 8-bit raw count
c_n^{ℓ}	NOAA-2 linear 8-bit raw count
CDF(X)	cumulative distribution function
F	interpolated probability level
G_i	gain of sensor i
lwc	liquid water content
m	occurrence corresponding to a particular probability level
N_{EFF}	effective filtered radiance
n_i	number of occurrences in the ith class interval
n(r)	number of cloud droplets cm^{-3} μm^{-1}
N_T	model radiance from cloud top into solid angle $\Delta\omega(\bar{\theta},\bar{\phi})$
N_X	model radiance from X-face of cloud into solid angle $\Delta\omega(\bar{\theta},\bar{\phi})$
N_Y	model radiance from Y-face of cloud into solid angle $\Delta\omega(\bar{\theta},\bar{\phi})$
$\bar{N}_{\Delta\omega(\bar{\theta},\bar{\phi})}$	area-averaged radiance into solid angle $\Delta\omega(\bar{\theta},\bar{\phi})$
O_i	offset of sensor i
P_i	power of sensor i
PL	probability level
$P(\alpha)$	scattering phase function
$PP(\alpha)$	cumulative probability number

PR	probability
r	droplet radius in microns or correlation coefficient
RN	random number
s	geometric distance
$\hat{s}$	unit vector in direction of viewer
$\hat{t}$	unit vector normal to cloud top
TA	total cloud area
TN	total number of occurrences in all class intervals
v_i	voltage of sensor i
x	highest class interval of at least one occurrence
X	X-axis
$\hat{x}$	unit vector normal to X-face of cloud
Y	Y-axis
$\hat{y}$	unit vector normal to Y-face of cloud
Z	Z-axis
α	scattering angle
β	volume scattering coefficient
γ	second scattering angle
λ	wavelength
ω	solid angle
ϕ	azimuth angle
τ	optical depth
θ	zenith angle

individual clouds. Differences between the scattering properties of an infinite cloud and a finite cloud are due to radiation entering and leaving through the sides of the finite cloud. Light exiting through the sides of a finite cloud results in a smaller magnitude of upward directional reflectance compared to the upward directional reflectance for an infinite cloud. The sides of a finite cloud are also responsible for producing an angular distribution of scattered light that is different from that found for an infinite cloud. The recognition of the radiative effects of cloud shape has a large impact on the approach of how, where and when to view cloud fields to properly observe their radiative characteristics, such as with satellites.

Satellite observations of cloud fields usually exhibit horizontal inhomogeneities within those cloud fields. If horizontal inhomogeneities are indicative of the presence of effects due to cloud shape, then the scattering effects of those cloud features could affect the satellite observations and interpretation of those observations. There are two objectives to this study to determine how cloud shape affects satellite observations and interpretation of those observations. The first objective is to investigate the effects of cloud shape on diurnal satellite observations of individual clouds and fields of clouds of varying horizontal homogeneity. The second objective is to investigate the effect of varying the satellite sensor spatial resolution on these diurnal satellite observations to determine if the observed phenomena are resolution dependent.

1.3 Approach

The first objective is carried out by first generating a simulated sequence of diurnal satellite observations for a theoretical finite and

infinite cloud for selected viewing geometries. Next, a diurnal sequence of high resolution visible satellite data that contains a field of clouds and conforms to the viewing geometries used in the theoretical sequences is selected. If the infrared data indicates that there is little change in the field or only minor changes that will not bias the results, the visible satellite data are statistically stratified and the results are compared to the previously generated theoretical diurnal variations of scattered light for an infinite and a finite cloud. The second objective entails degrading the high resolution data to low resolution through the use of a spatial averaging scheme and performing the same type of analysis done in objective one.

Chapter 2

SIMULATED DIURNAL RADIANCE PATTERNS OF A FINITE AND AN INFINITE CLOUD

2.1 Model Description

The model used in this study for simulating the interaction of solar radiation with a cloud is based on the Monte Carlo method which has been described in detail by Cashwell and Everett (1959). This method simulates the paths of individual photons through a cloud by using random numbers in conjunction with probability distributions for computing the scattering angle of a photon when an interaction occurs and also for computing the distance travelled by a photon between interactions. Kattawar and Plass (1971) and Danielson et al. (1969) have used the Monte Carlo method to compute scattering in semi-infinite horizontal cloud layers. Busygin et al. (1973) and McKee and Cox (1974, 1976) used the Monte Carlo method to calculate scattering in finite-shaped clouds. The version of the model used in this study is described in McKee and Cox (1974, 1976) and DeMaria and McKee (1979). A brief description of the model will be given to familiarize the reader with this particular model.

The Monte Carlo method is a direct simulation of the radiative processes inside a cloud. A three-dimensional set of boundaries are defined for the limits of the cloud and then photons are allowed to enter the cloud from a specific direction. The distance each photon travels until a scattering event occurs is determined and then the new direction of travel is selected from the appropriate phase function.

This process is repeated until the photon escapes through a cloud boundary. The distance between interactions and the phase function are determined by specified cloud microphysical properties and the wavelength of the interacting radiation.

The present model considers an isolated cloud with no absorption, no surrounding atmosphere and no ground reflection. Consequently, the only processes simulated are the distance travelled by each photon between scattering events and the change in direction caused by each interaction.

The cloud is assumed to be homogeneous and comprised of water droplets with a size distribution of

$$n(r) = 2.373\ r^6 \exp(-1.5r) \qquad (2.1)$$

where r is the droplet radius in microns and $n(r)$ is the number of droplets $cm^{-3}\ \mu m^{-1}$. This distribution was obtained from Diermendjian (1969) and is referred to as a type C1 distribution which is a model for a cumulus cloud. For 100 droplets cm^{-3}, the C1 distribution results in a liquid water content (lwc) of $0.063\ g\ m^{-3}$. The volume scattering coefficient (β) is dependent on the wavelength (λ) of the interacting radiation, the droplet distribution, and the liquid water content. The value of β is $16.73\ km^{-1}$ for a wavelength of $0.7\ \mu m$, the C1 distribution and a liquid water content of $0.063\ g\ m^{-3}$. Since the cloud is assumed to be homogeneous, optical depth (τ) is linearly related to geometric distance (s) through the relation

$$\tau = \int_0^s \beta ds \text{ or } \tau = \beta s. \qquad (2.2)$$

For the C1 distribution and wavelength of $0.7\ \mu m$, the volume scattering coefficient for any liquid water content amount is directly

proportional to the volume scattering coefficient of $16.73\ km^{-1}$ for liquid water content of $0.063\ g\ m^{-3}$ or

$$\frac{\beta_{lwc}}{lwc} = \frac{16.73\ km^{-1}}{0.063\ g\ m^{-3}} \qquad (2.3)$$

Therefore, from Eq. (2.2) a cloud 1.5 km thick would have an optical depth of 25.0 for a liquid water content of $0.063\ g\ m^{-3}$. The same size cloud with a liquid water content of $0.185\ g\ m^{-3}$ would have a volume scattering coefficient of 49.1 from Eq. (2.3) and an optical depth (τ) of 73.5 from Eq. (2.2).

The distance that a photon travels between scattering events is directly simulated in the model since the fraction of radiation transmitted through a given distance ($e^{-\tau}$) is also the probability that a photon will travel through that same distance without an interaction (PR). This is expressed by

$$e^{-\tau} = \exp\left(-\int_0^s \beta ds\right) = PR \quad . \qquad (2.4)$$

A random number (RN) between zero and one is chosen for the probability PR, and the distance to the next scattering event(s) is calculated by determining the upper limit of integration of

$$\tau = -\ln(1-RN) = \int_0^s \beta ds \quad . \qquad (2.5)$$

The single scattering phase function $P(\alpha)$ defines the angular distribution of the radiation following a scattering event. The scattering angle α is measured from the direction of propogation before the scatter to the direction after the scatter. The phase function is normalized so that the integral over all solid angles equals one, i.e.,

$$\int_0^{2\pi} \int_0^{\pi} P(\alpha) \sin \alpha \, d\alpha \, d\gamma = 1 \, , \tag{2.6}$$

where γ is the angle of rotation about the original direction of propagation. Since the phase function is independent of γ, Eq. (2.6) reduces to

$$2\pi \int_0^{\pi} P(\alpha) \sin \alpha \, d\alpha = 1 \, . \tag{2.7}$$

The probability of a photon being scattered between 0 and α ($PP(\alpha)$) is then given by

$$PP(\alpha) = 2\pi \int_0^{\alpha} P(\alpha') \sin \alpha' \, d\alpha' \, , \tag{2.8}$$

where primes indicate a specific angular interval of integration. The phase function is characterized by a strong forward scattering peak as shown in Figure 1 which shows a 50 percent probability of a photon scattering between 0 and 10 degrees. The scattering angle (α) is computed from Eq. (2.8) in the same manner that the distance between scattering events was calculated in Eq. (2.5). A random number between zero and one is selected for $PP(\alpha)$ and the upper limit of integration is solved for in Eq. (2.8), which is the scattering angle α. The second angle γ, which along with angle α specify the new direction of travel, is chosen randomly between 0 and 2π.

The cloud geometry along with the coordinate system used in the model are shown in Figure 2. The incident sunlight is plane parallel and is always in the Y-Z plane, which restricts the sunlight to the slab top and/or the +Y face of the cubic cloud. The direction of travel of exiting radiation is specified by a zenith angle θ measured from the +Z axis and an azimuth angle ϕ measured from the -Y axis. A ϕ value of 0 is opposite the sun and a ϕ angle of π is towards the sun.

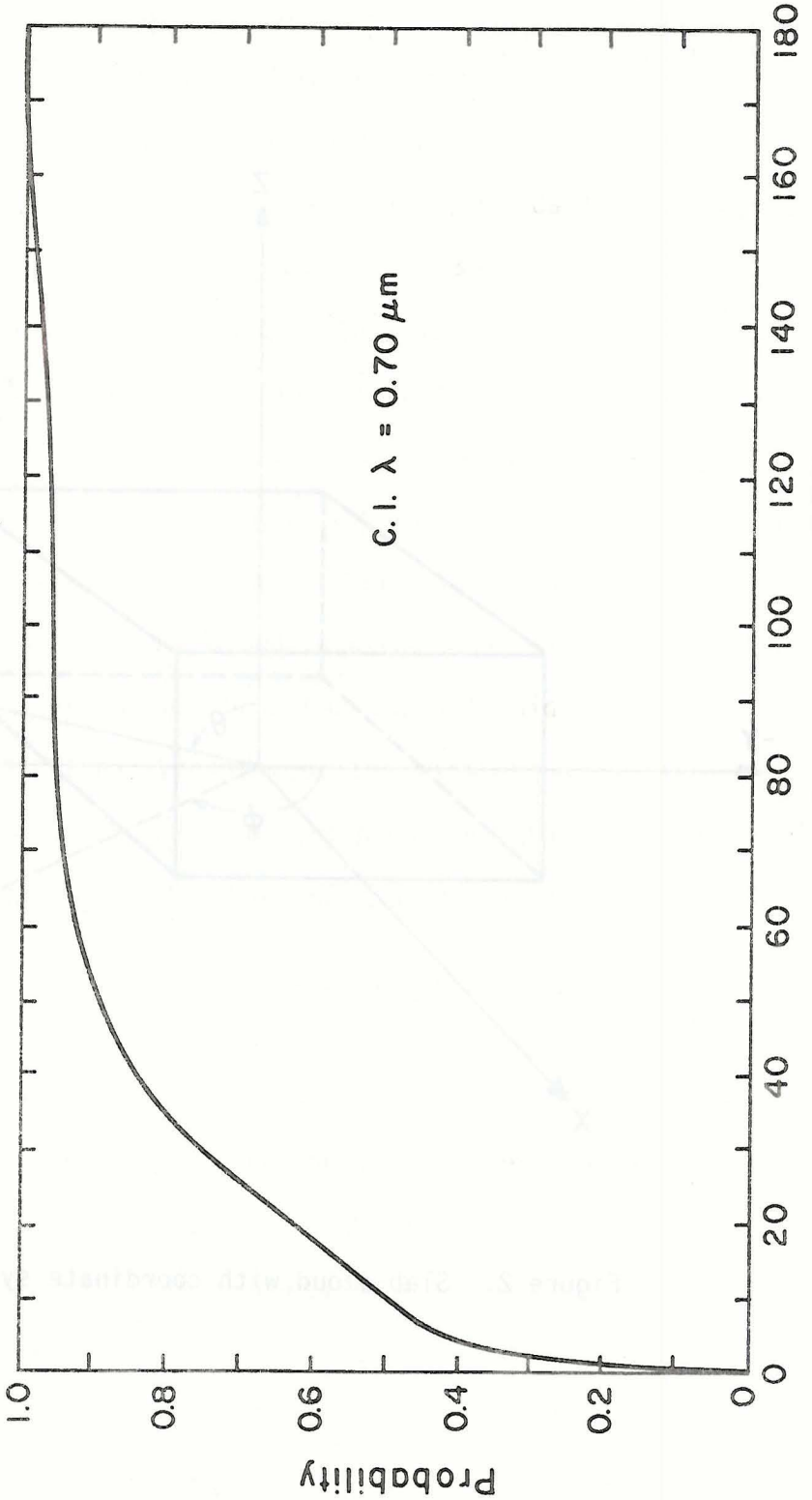

Figure 1. Cumulative distribution function for C1 model at $\lambda = 0.7$ μm (from DeMaria and McKee, 1979).

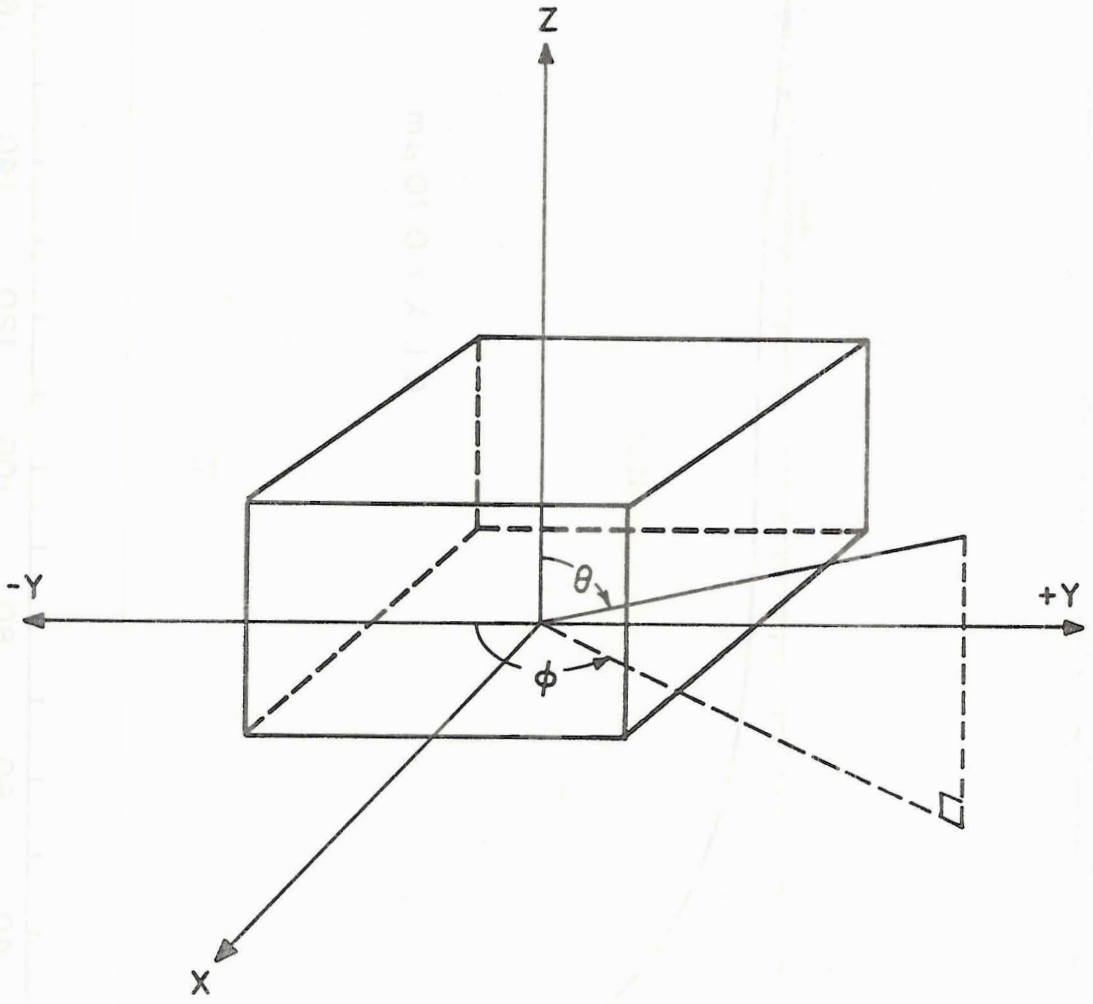

Figure 2. Slab cloud with coordinate system.

The model output gives relative radiance values for each of the slab faces averaged over a finite solid angle $\Delta\omega$, where

$$\Delta\omega = \Delta(\cos\theta)\Delta\phi \tag{2.9}$$

for $\Delta(\cos\theta) = 0.05$ and $\Delta\phi = \pi/12$. All radiances are relative to an incident solar irradiance of π.

The accuracy of the computed radiances depends on the number of photons processed through a given simulation. The model simulations for this study were performed with 80,000 photons being processed through a given cloud. This large number of photons significantly reduced the noise levels in the model radiances.

2.2 Adjustment of Model Radiances to Simulate Satellite Data

The Monte Carlo model was used to simulate the angular distribution of scattered light from an infinite and a finite cloud. An infinite cloud has a finite vertical extent and an effectively infinite horizontal extent. Photons enter the top of the cloud and exit through either the top or bottom of the cloud. A finite cloud has photons enter the top and/or one side of the cloud and they are allowed to exit any of the six faces of the cloud. Before these model simulations can be compared to real satellite data, however, careful adjustments to some of these model radiances are necessary due to the sampling nature of a satellite sensor.

The sensor on a satellite cannot resolve any details or inhomogeneities within an observation that are smaller than that sensor's highest resolution. The sensor returns one value for each field of view (FOV) which represents an area-weighted average of the different brightnesses of the various cloud field elements that lie

within that FOV: cloud top, cloud side and the earth's surface. A satellite observation (or pixel) of an infinite cloud (Figure 3a) would have the entire FOV filled with cloud and in particular with only the top of the cloud. Since the cloud fills the FOV and is homogeneous, no adjustment of the infinite cloud Monte Carlo model radiances needs to be made to simulate a satellite observation. A satellite observation of a finite cubic cloud (Figure 3b) that has the FOV exactly filled by the cloud contains contributions from both the top and observed sides of the cloud for all satellite viewing angles (θ) except $\theta = 0°$. Since the cloud that lies within the FOV is not homogeneous (both top and sides visible to satellite), simulating a satellite observation (or pixel) of a finite cloud requires area-averaging the Monte Carlo model radiances from the top and appropriate sides.

This area-averaging of the finite cubic cloud model radiances is accomplished by first determining the total cloud area (TA) visible from a given solid angle box $\Delta\omega$ centered on $(\bar{\theta},\bar{\phi})$ by

$$TA_{\Delta\omega(\bar{\theta},\bar{\phi})} = A_T(\hat{t}\cdot\hat{s}) + A_X(\hat{x}\cdot\hat{s}) + A_Y(\hat{y}\cdot\hat{s}) \quad , \tag{2.10}$$

where A_T, A_X, and A_Y are the areas of the top, X, and Y faces of the cloud; $\hat{t}$, $\hat{x}$, and $\hat{y}$ are the unit vectors perpendicular to the respective cloud faces; and $\hat{s}$ is the unit vector in the direction specified by $(\bar{\theta},\bar{\phi})$. The dot products of $\hat{s}$ and the three other unit vectors are approximated by

$$\hat{t}\cdot\hat{s} \cong \overline{\cos\theta} \quad , \tag{2.11}$$

$$\hat{x}\cdot\hat{s} \cong \overline{\sin\theta}\ \overline{\sin\phi} \quad , \tag{2.12}$$

$$\hat{y}\cdot\hat{s} \cong \overline{\sin\theta}\ \overline{\cos\phi} \quad , \tag{2.13}$$

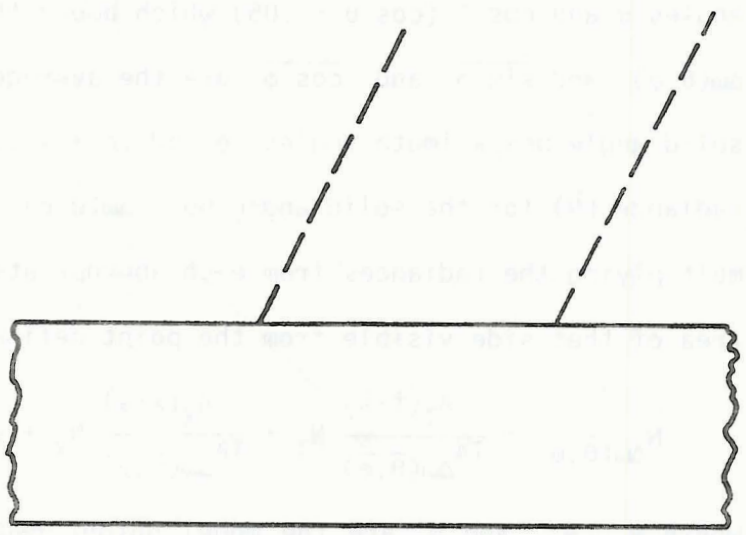

a. Infinite Cloud

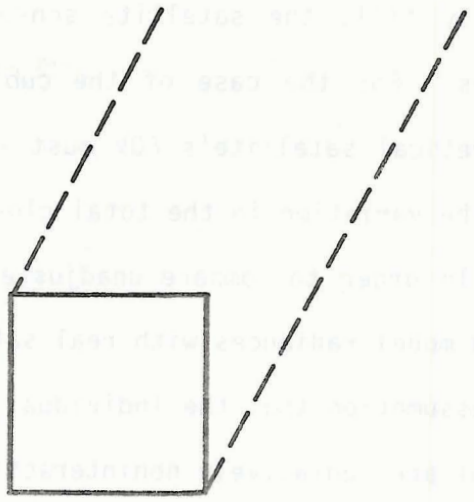

b. Finite Cloud

Figure 3. Examples of a single satellite observation of a theoretical infinite (a) and finite cubic cloud (b).

where $\overline{\cos\,\theta}$ and $\overline{\sin\,\theta}$ are the average cosine and sine of the zenith angles θ and $\cos^{-1}(\cos\,\theta - .05)$ which bound the solid angle box $\Delta\omega(\bar{\theta},\bar{\phi})$; and $\overline{\sin\,\phi}$ and $\overline{\cos\,\phi}$ are the average sine and cosine of the solid angle box azimuth angles ϕ and $(\phi + \pi/12)$. The area-averaged radiance $(\bar{N})$ for the solid angle box $\Delta\omega(\bar{\theta},\bar{\phi})$ is then calculated by multiplying the radiances from each appropriate side by the fractional area of that side visible from the point defined by $(\bar{\theta},\bar{\phi})$:

$$\bar{N}_{\Delta\omega(\bar{\theta},\bar{\phi})} = \frac{A_T(\hat{t}\cdot\hat{s})}{\overline{TA}_{\Delta\omega(\bar{\theta},\bar{\phi})}} N_T + \frac{A_X(\hat{x}\cdot\hat{s})}{\overline{TA}_{\Delta\omega(\bar{\theta},\bar{\phi})}} N_X + \frac{A_Y(\hat{y}\cdot\hat{s})}{\overline{TA}_{\Delta\omega(\bar{\theta},\bar{\phi})}} N_Y \qquad (2.14)$$

where N_T, N_X, and N_Y are the model output radiances from the top, X, and Y faces, respectively, into the solid angle box $\Delta\omega(\bar{\theta},\bar{\phi})$. This area-averaging scheme assumes that the theoretical finite cubic cloud exactly fills the satellite sensor's FOV for all possible viewing angles. For the case of the cubic cloud used in this study, the theoretical satellite's FOV must vary by almost 71 percent to account for the variation in the total cloud area viewed.

In order to compare unadjusted infinite cloud and adjusted finite cloud model radiances with real satellite observations of cloud fields, the assumption that the individual cloud elements in the observed cloud fields are radiatively noninteracting must be made. This assumption is necessary since the radiative behavior of a field of clouds is being compared to an individual theoretical cloud which is void of cloud interactions. Also, it is necessary to use only observed cloud fields which are, on the whole, close to a steady-state condition throughout the day. This is necessary because large changes in cloud cover or thickness could substantially affect the diurnal variation in observed

radiance for that cloud field. Some changes in the microphysical structure of the observed clouds may occur during the day, but McKee and Klehr (1978) demonstrated that such changes will change the reflected radiances by only a few percent.

2.3 Model Results Simulating Satellite Observations

Simulated upwelling radiances from an infinite cloud and a finite cubic cloud for solar zenith illumination angles (θ_0) of 0, 15, 30, 45 and 60° were calculated using the Monte Carlo model. Two sets of simulations were performed with clouds of optical depth 73.5 and 20.0 (Figures 5 and 6, respectively). Both figures show the theoretical diurnal variation of scattered light observed by satellite for an infinite and finite cubic cloud from two different viewing geometries. The clouds lie on the equator at the equinox so that the sun passes directly overhead at local noon (Figure 4). The two viewing angles are in the plane of the cloud and sun at zenith angles of $\theta = 0°$ and an average angle ($\bar{\theta}$) from 18 to 31°, $\phi = 22°$, with the angle measured westward from zenith allowing the viewer to see only the top and west face of the cloud. This interval of viewing angles was chosen since the SMS-1 satellite is situated over the equator at 45°W longitude and the GATE sector covers the longitutinal interval 50°W to 5°W, allowing for a 40° longitudinal range in satellite viewing angles along the equatorial plane to the east of the satellite sub-point.

Figure 5 depicts the theoretical diurnal variation of upwelling radiance for an optically thick ($\tau = 73.5$) infinite and finte cubic cloud from two different viewing geometries. When looking straight down at an infinite cloud ($\theta = 0°$), the diurnal variation of radiance is symmetric about local noon when the peak radiance is observed. The

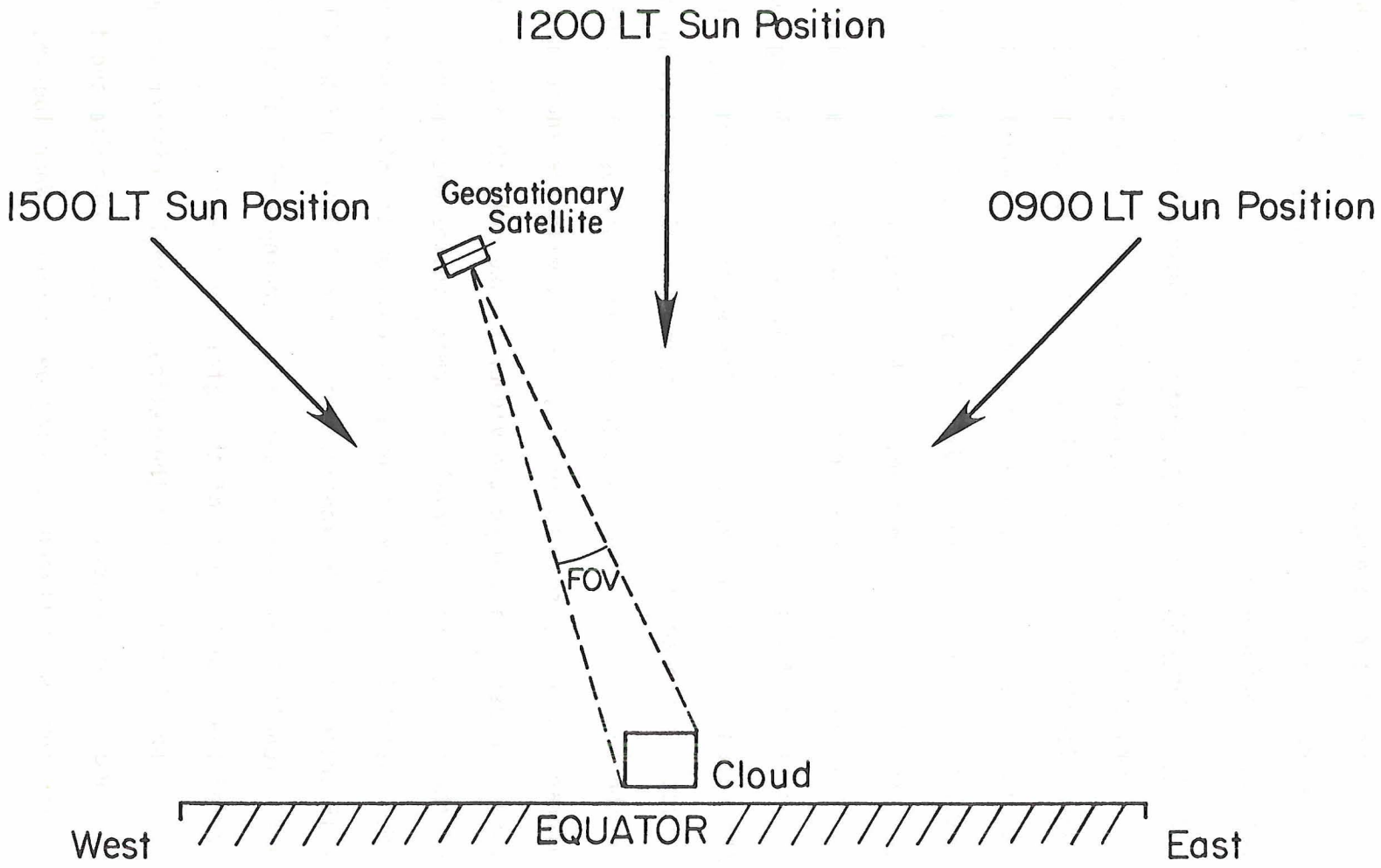

Figure 4. Relative positions of the satellite and a finite cloud situated in the equatorial plane at the equinox.

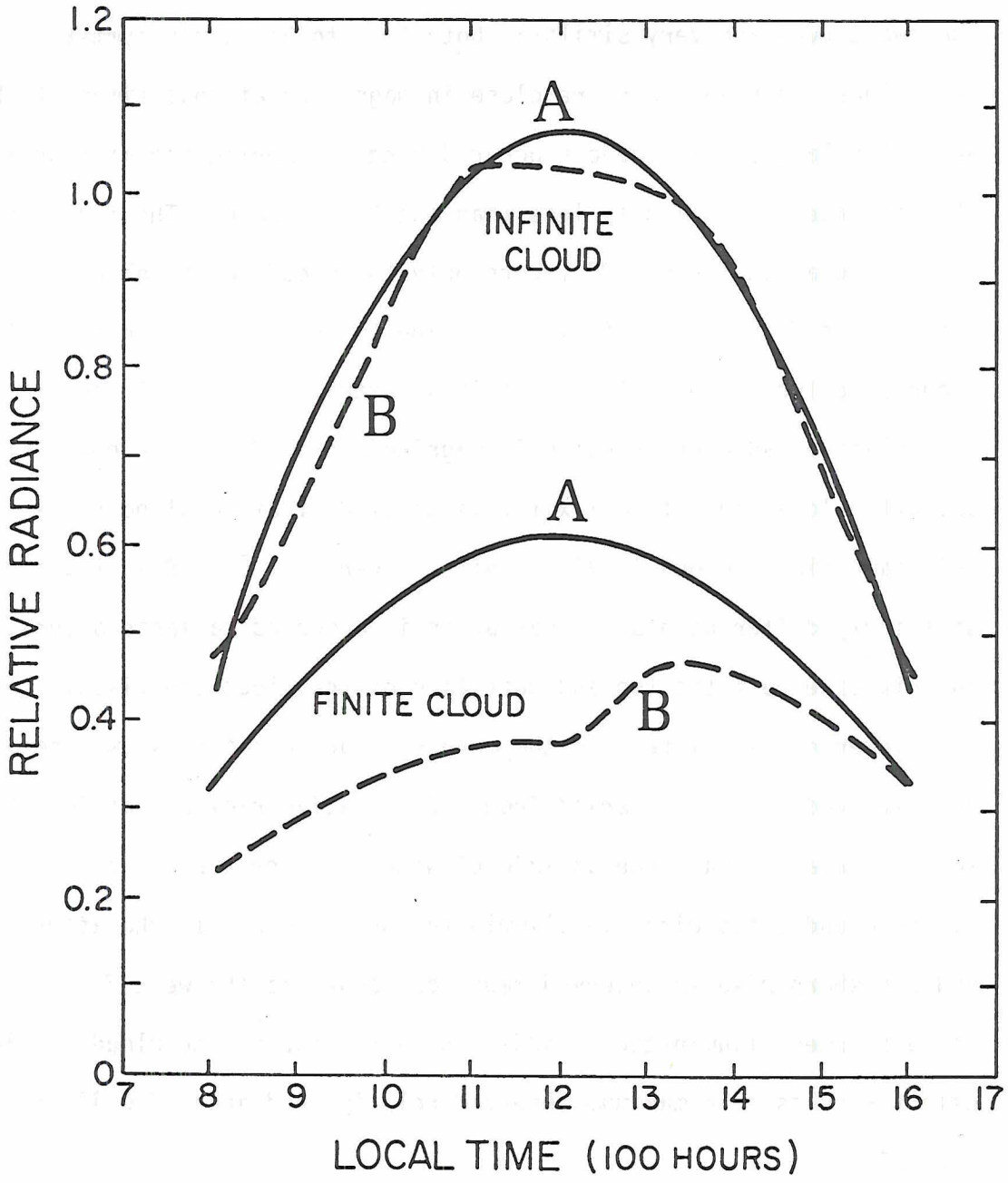

Figure 5. Theoretical diurnal variation of upwelling radiance as viewed by satellite for an optically thick ($\tau = 73.5$) infinite cloud (top two curves) and finite cubic cloud (bottom two curves) from $\theta = 0°$ (A) and $\bar{\theta} = 18 \rightarrow 31°$, $\phi = 22°$ (B).

relative radiances range in magnitude from 0.40 four hours before and after noon to a peak value of 1.07 at local noon. When viewing the same infinite cloud at an average zenith angle $\bar{\theta} = 18 \rightarrow 31°$, $\phi = 22°$, a slightly different diurnal radiance pattern is observed. Overall, the two curves are very similar: both tend to be nearly symmetric about local noon and both are close in magnitude at most times of the day. The largest differences occur during mid-moring and at noon when the radiances are slightly less than the $\theta = 0°$ case. The finite cubic cloud simulation for $\theta = 0°$ (where only the cloud top is observed) depicted in Figure 5 is similar in shape to what is seen in the infinite cloud case for $\theta = 0°$. The curve is symmetric about local noon with the relative radiances ranging in magnitude from 0.33 four hours before and after local noon to a maximum value of 0.61 at local noon. When this same finite cloud is viewed off the vertical $\bar{\theta} = 18 \rightarrow 31°$, a strikingly different diurnal variation in observed radiance occurs. In this case both the top and west face of the cloud are visible to the viewer or satellite. In the morning hours a rather slow rise in relative radiance is observed from 0.24 relative radiance at 0800 LT to 0.38 relative radiance at 1200 LT with only the top and east face of the cloud being directly illuminated by the sun. In the afternoon hours a sharp rise in observed radiance occurs as the west face of the cloud becomes illuminated in addition to the top of the cloud. This effect results in a maximum observed relative radiance of 0.47 at 1330 LT.

Figure 6 depicts the theoretical diurnal variation of upwelling radiance for an infinite and a finite cubic cloud each with an optical depth of 20.0 and from the same two viewing geometries discussed in

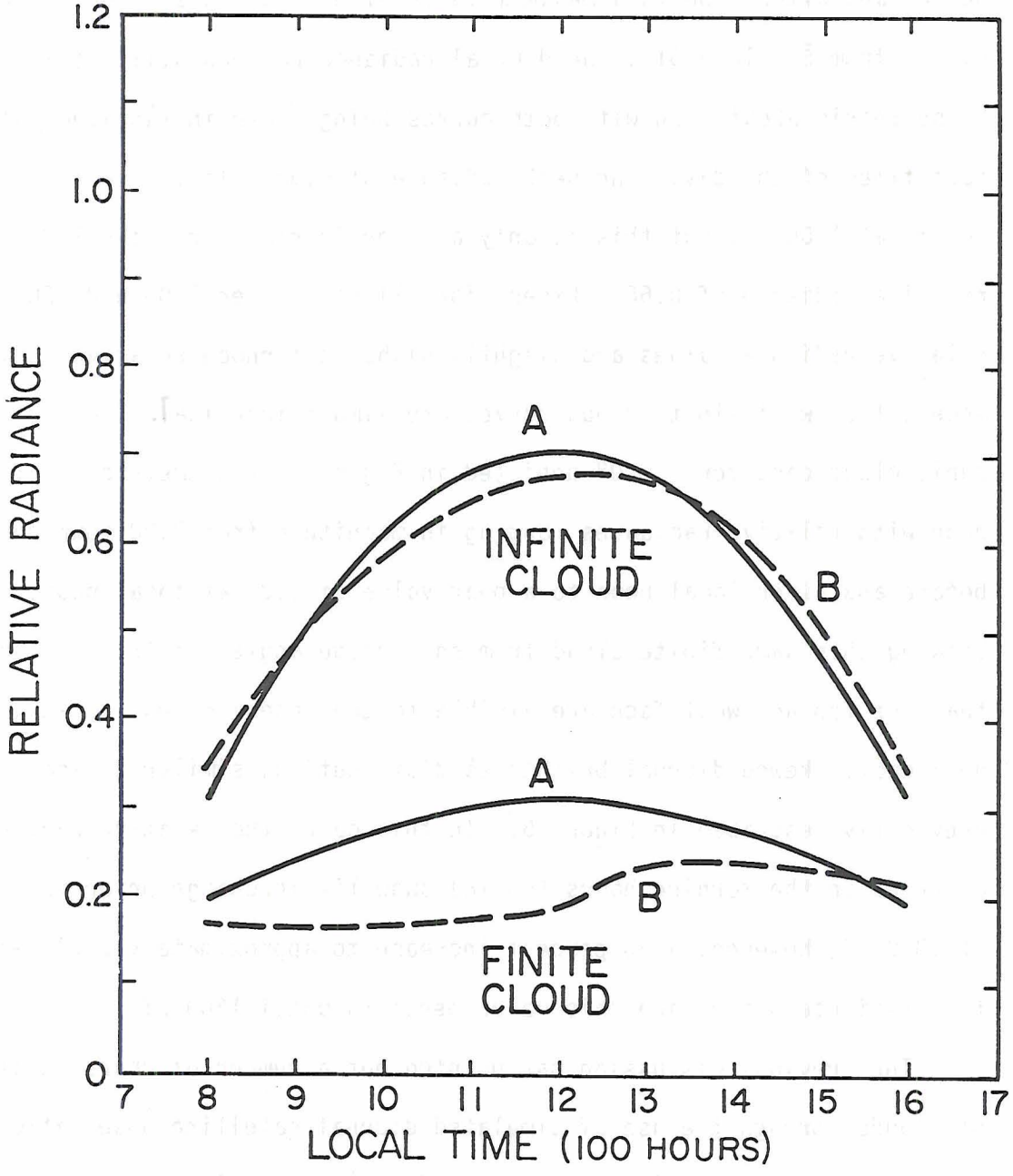

Figure 6. Same as Figure 5 except τ = 20.

Figure 5. The $\theta = 0°$ infinite cloud case is symmetric about local noon with relative radiances ranging in magnitude from 0.32 four hours before and after noon to a maximum value of 0.71 at local noon. When viewed from $\bar{\theta} = 18 \rightarrow 31°$, the diurnal radiance pattern still tends to be symmetric about noon with both curves being close in magnitude at most times of the day. The peak radiance of 0.68 relative radiance occurs at 1300 LT, but this is only a minor increase from the 1100 LT relative radiance of 0.66. Except for slightly lower 1100 and 1200 LT relative radiance values and slightly higher afternoon relative radiances, the two infinite cloud curves are almost identical. The finite cubic cloud case for $\theta = 0°$ depicted in Figure 6 is symmetric about noon with relative radiances ranging in magnitude from 0.20 four hours before and after local noon to a peak value of 0.32 at local noon. Viewing this same finite cloud from an average angle $\bar{\theta} = 18 \rightarrow 31°$ so that the top and west face are visible to the observer results in a noticeably skewed diurnal brightness distribution, similar to what was previously described in Figure 5. In this case, the relative radiances observed in the morning hours (~0.18) show little change prior to noon. At 1300 LT, however, a 33 percent increase to approximately 0.24 relative radiance occurs and this value persists until 1600 LT.

The previous discussion has pointed out a number of characteristics of clouds through the use of simulated diurnal satellite observations. The first characteristic is that an infinite cloud viewed anywhere in the interval $\theta = 0°$ to $\bar{\theta} = 18 \rightarrow 31°$ (measured westward from zenith) has a theoretical diurnal radiance pattern that is essentially symmetric about noon, has a sharp rise (fall) in the morning (afternoon) hours,

and has a maximum radiance value at or very close to noon which is driven by the diurnal variation of the incident solar radiation. The second characteristic is that a finite cloud (or a field of radiatively noninteracting finite clouds) viewed at $\theta = 0°$ has a theoretical diurnal radiance pattern that is also symmetric about noon with a peak value occurring at local noon. The third characteristic is that when viewing finite clouds from an average angle $\bar{\theta} = 18 \rightarrow 31°$, a prominent afternoon peak in radiance is observed that is at least 30 percent greater than the 1100 LT radiance vlaue. This is characteristically unique to the finite cloud in that the duration of these higher radiances is for three or more hours in the afternoon and the percent increase in afternoon radiances is far greater than any observed in the two infinite cloud cases.

Significant differences between the theoretical diurnal variation in observed radiances for an infinite and finite cubic cloud for $\bar{\theta} = 18 \rightarrow 31°$ are due to cloud shape as both the cloud top and west face become illuminated in the afternoon in the finite cloud case. Similar diurnal radiance patterns should be apparent in satellite observations of inhomogeneous cloud fields if those horizontal inhomogeneities are indicative of the presence of effects of cloud shape.

Chapter 3

SATELLITE DATA DESCRIPTION AND PROCESSING

The satellite data used in this study for comparison with the simulated satellite observations is 1974 GARP Atlantic Tropical Experiment (GATE) satellite data which was collected by the first Synchronous Meteorological Satellite (SMS-1) and described by Smith and Vonder Haar (1976). This data set was chosen for two reasons. The first is that SMS-1 was a geostationary satellite that collected both visible and infrared (IR) data throughout the day, providing a diurnal sequence of observations from a fixed position. The second reason was the cheap and easy accessability of the satellite data at the National Center for Atmospheric Research (NCAR) Computing Facility where all of the computer processing for this study was performed.

3.1 Satellite Characteristics

SMS-1 was a geostationary satellite orbiting at an altitude of approximately 35,000 km and positioned at 0° latitude and 45° W longitude. The satellite collected full-disc data every 30 minutes during GATE for the period covering June 27 to September 20, 1974. The IR data were taken starting at 0000 GMT and ending at 2300 GMT, providing 24 hours of IR coverage. The visible data were taken starting at 0800 GMT and ending at 1900 GMT, providing 12 hours of visible coverage.

3.2 Satellite Data Set Description

The image scanning device carried aboard SMS-1 is called a Visible Infrared Spin-Scan Radiometer (VISSR) which contains eight visible sensors in the spectral range of 0.55 μm to 0.75 μm and two redundant IR sensors in the range 10.5 μm to 12.5 μm. The VISSR permits high spatial resolution, narrow spectral resolution and small solid angle measurements of reflected solar radiation and emitted IR radiation from the top of the atmosphere. The FOV of a single IR sensor is approximately 4 by 4 n. mi at the satellite sub-point (SSP). Only one IR sensor is used for any given image. The FOV of a single visible sensor is approximately 1/2 by 1/2 n. mi resolution at the SSP.

The voltage responses of the eight visible sensor photomultipliers are assumed to be linear with incident energy

$$P_i = G_i (V_i - O_i) \tag{3.1}$$

where P_i is power in watts, G_i is the gain of a given sensor in watts per volt, V_i is voltage ($0 \leq V_i \leq 5$), O_i is the voltage offset and subscript i denotes one of the eight sensors. The voltage offset for each sensor is assumed to be negligible, less than 0.03 volts. The conversion of voltage to raw counts that are returned by the satellite is nonlinear and approximates a square root function

$$C_i = 28.1(V_i)^{\frac{1}{2}} \tag{3.2}$$

where C_i is a 6-bit raw count ($0 \leq C_i \leq 63$) for sensor i and 28.1 is a constant. This nonlinear voltage-to-count conversion was used to keep the signal-to-noise ratio linear with respect to counts; there is an increase in signal-to-noise ratio with respect to increasing incident light energy (see Design Review Report--Visible Infrared

Spin-Scan Radiometer (VISSR) for a Synchronous Meteorological Satellite (SMS), published by Santa Barbara Research Center (1972)).

Full resolution IR data (4 by 4 n. mi) was collected and stored on magnetic tape at the original data collection site; however, reduced resolutions visible data (2 by 2 n. mi) produced by the averaging scheme illustrated in Figure 7 was stored on tape. It should be noted that the resultant 2 n. mi resolution raw count data ($C_s^{n\ell}$) are not true averages since the square root digitization process was not taken into account.

The full resolution IR and reduced resolution visible satellite data for the GATE sector outlined in Figure 8 were extracted from the original full-disc image digital recordings by Smith and Vonder Haar (1976). These raw data do not conform exactly to earth latitude and longitude coordinates and Smith et al. (1976) elected to bypass earth-locating the raw data since to do so would have created discontinuities in the data signal and would have been very costly.

3.3 Calibration of SMS-1 Visible Satellite Data

Since no prelaunch photometric data from the SMS-1 Flight-1 VISSR detector is available for calibration purposes, Smith and Loranger (1977) devised a calibration procedure which utilized the NOAA-2 scanning radiometer (SR) model F-15 aboard a polar-orbiting satellite operational during 1974 GATE to cross-calibrate the SMS-1 sensor. This is possible since the NOAA-2 SR was photometrically calibrated prior to launch as discussed by Jones et al. (1965) and Smith and Loranger (1977). The relative spectral response characteristics of the NOAA-2 SR and the SMS-1 VISSR (eight detector mean) shown in Figure 9 depict the similar normalized spectral responses of the two instruments. The

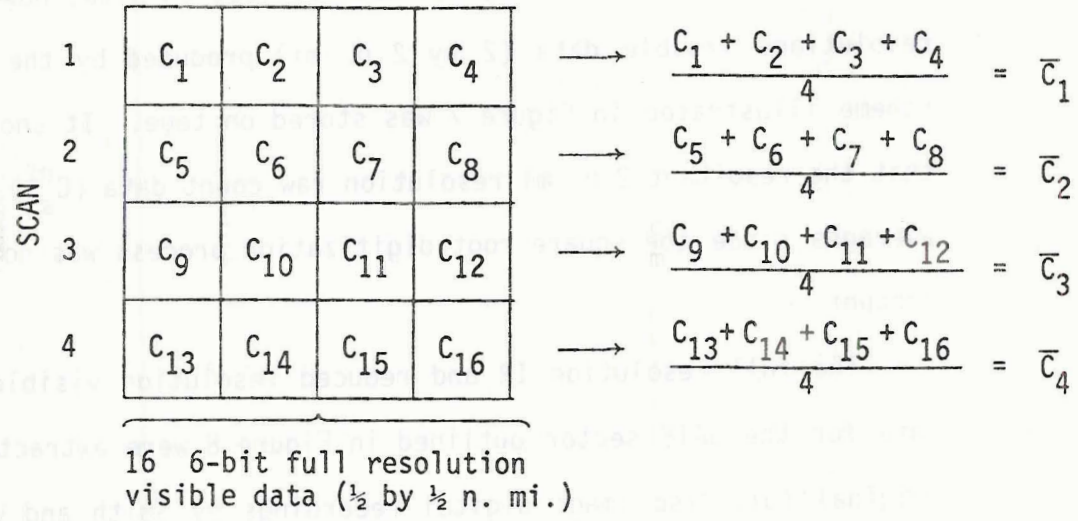

$$C_{s\,(2\text{ n. mi})}^{n\ell} = \sum_{i=1}^{4} \overline{C}_i \ ,$$

where $C_s^{n\ell}$ is 8-bit data $(0 \leq C_s^{n\ell} \leq 255)$.

Figure 7. Averaging scheme used to reduce ½ n. mi. resolution 6-bit visible data to 2 n. mi resolution 8-bit data.

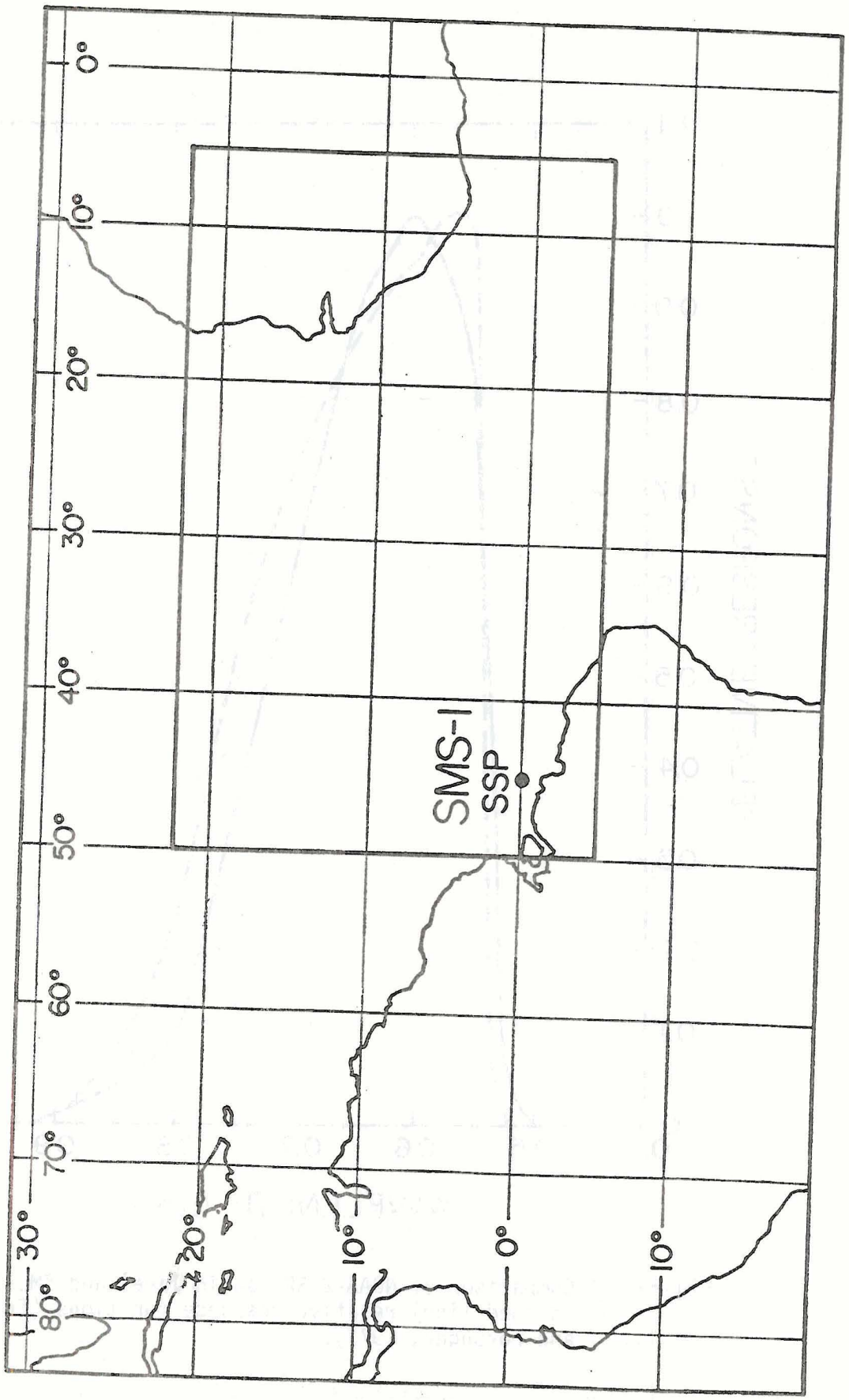

Figure 8. GATE sector and SMS-1 satellite subpoint (SSP).

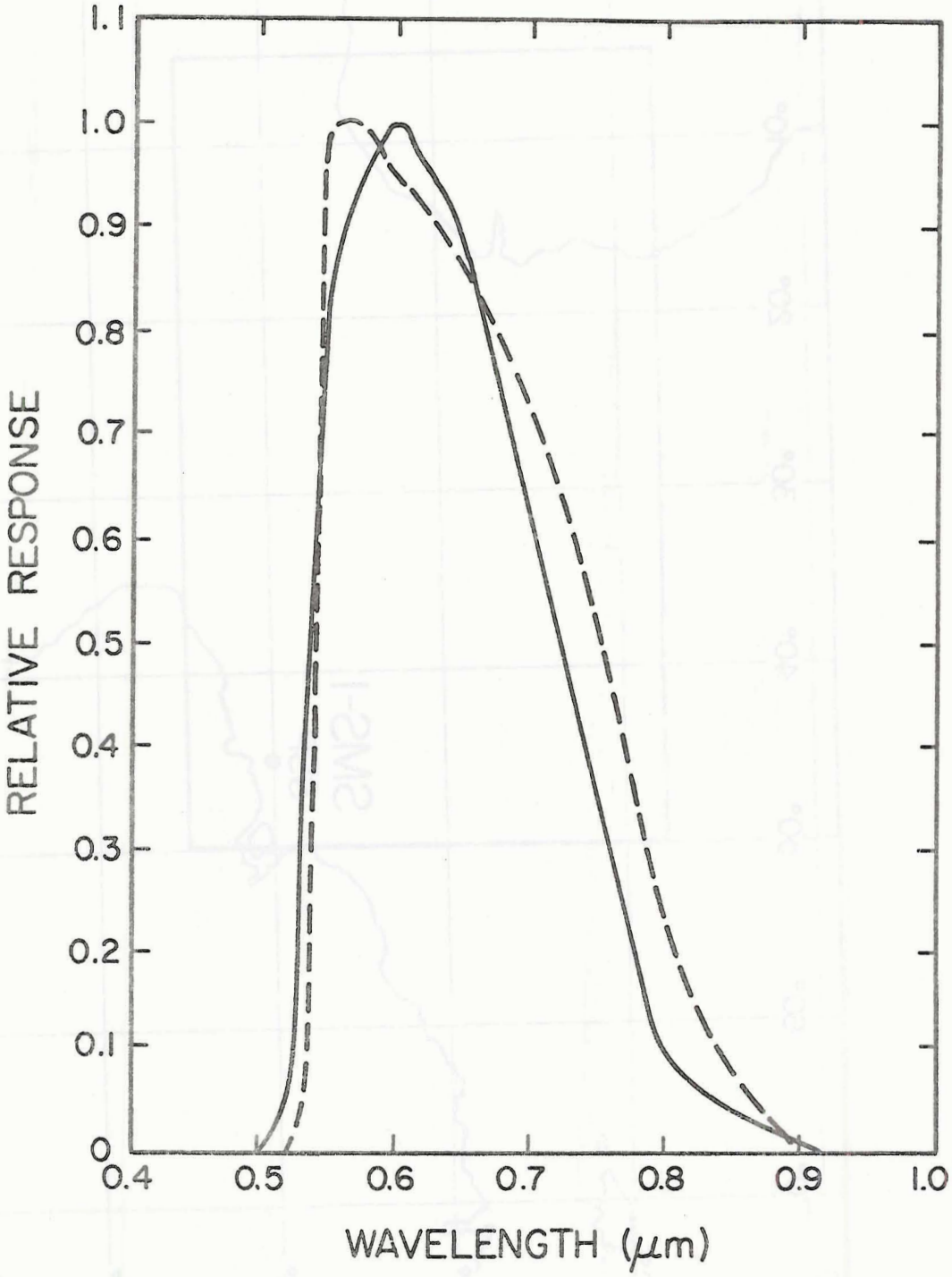

Figure 9. Comparison of NOAA-2 SR (solid line) and SMS-1 VISSR (dashed line) relative response functions (from Smith and Loranger, 1977).

following discussion on the satellite cross-calibration is based on Smith and Loranger (1977).

Cross-calibration was achieved by determining a linear regression relationship between a set of co-located measurements in space and time from NOAA-2 and SMS-1. The NOAA-2 SR sensor voltage responses and raw count scale are both linear with respect to incident radiation. As seen earlier in Eq. (3.2), the SMS-1 shortwave raw count data is not linear with voltage, even though the voltage outputs were linear with incident energy. These nonlinear SMS-1 raw count data were rescaled to a normalized linear 8-bit raw count scale equivalent to that used for the NOAA-2 digitization process by

$$c_s^{\ell} = 254.0 \left[\frac{c_s^{n\ell}}{255.0} \right]^2 \tag{3.3}$$

where c_s^{ℓ} is the linearized SMS-1 8-bit raw count, $c_s^{n\ell}$ is the nonlinear 8-bit raw count, 255.0 is the maximum SMS-1 8-bit raw count, and 254.0 is a scaling constant to scale the data to the 8-bit count scale used for the NOAA-2 digitization process.

The next step is to co-navigate simultaneous separate observations by each satellite of the same area on the earth's surface such that each pixel of data from one satellite is looking at approximately the same location as the corresponding pixel of the other satellite. The data sets selected by Smith and Loranger (1977) for co-navigation were taken on September 17, 1974 near 1000 GMT as the NOAA-2 polar orbiter was descending toward the equator and the SMS-1 satellite was in a geostationary position over the equator at 45° W. The region bounded by 19° N to 1° S and 12.5° W to 35° W was used for the analysis (Figure 10). The area of simultaneous observations in Figure 10 is

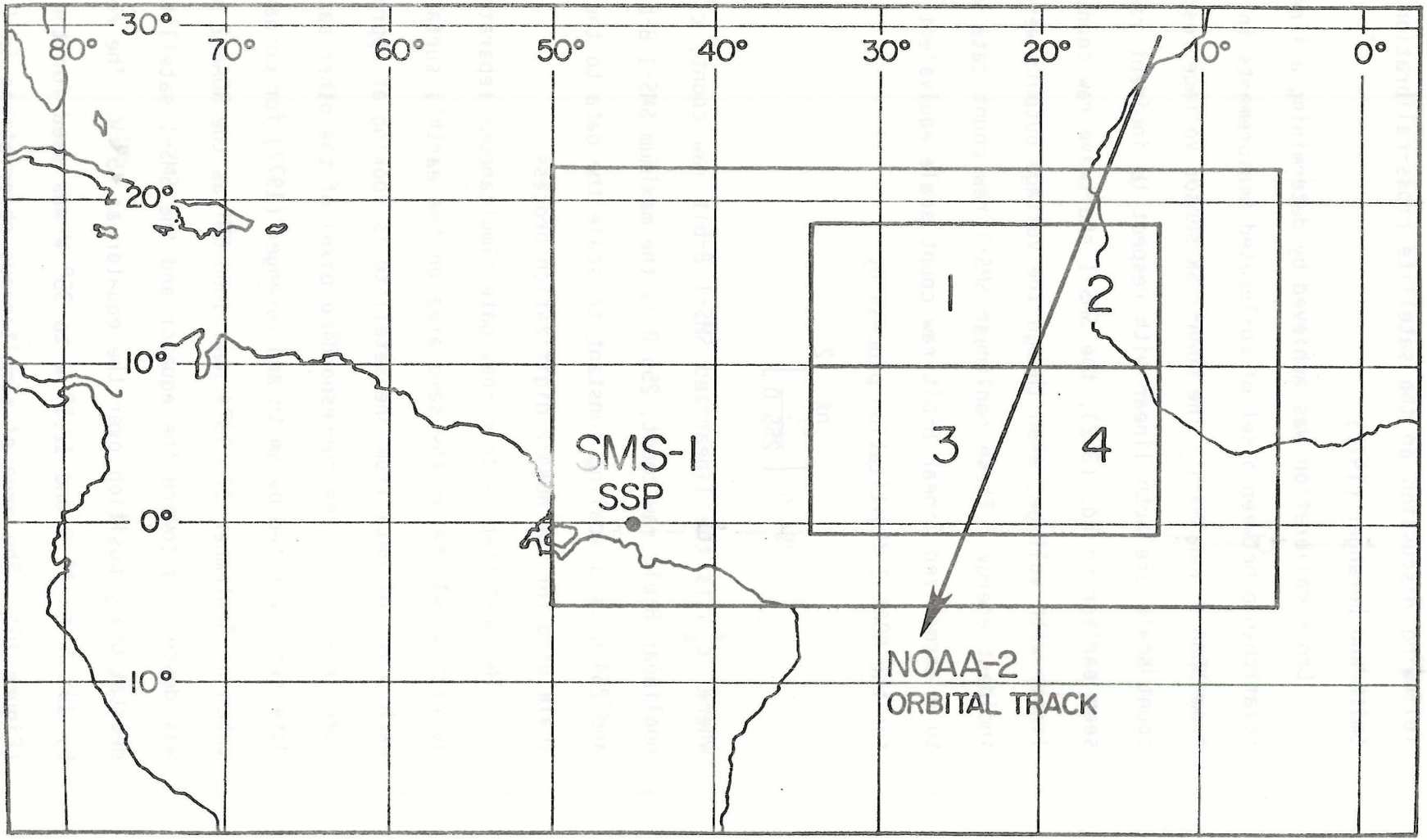

Figure 10. GATE sector and the four regions of simultaneous measurements by SMS-1 and NOAA-2 on September 17, 1974 near 1000 GMT.

divided up into four areas since both satellites would be monitoring forward scatter to the east of the NOAA-2 orbital track (areas 2 and 4) but only SMS-1 would monitor forward scatter to the west of the orbital track of NOAA-2 (areas 1 and 3). The two sets of data were then remapped to identical earth coordinates with spatial errors of ±1 pixel (±4 n. mi). Correlation coefficients between the SMS-1 and NOAA-2 data sets were calculated for each region by

$$r_{(c_n^{\ell}, c_s^{\ell})} = (\overline{c_n^{\ell} c_s^{\ell}} - \overline{c_n^{\ell}}\,\overline{c_s^{\ell}})[(\overline{(c_n^{\ell})^2} - \overline{c_n^{\ell}}\,\overline{c_n^{\ell}})(\overline{(c_s^{\ell})^2} - \overline{c_s^{\ell}}\,\overline{c_s^{\ell}})]^{-1/2} \quad (3.4)$$

where c_n^{ℓ} denotes saturation free NOAA-2 values, c_s^{ℓ} denotes SMS-1 values and bars denote mean quantities. The results shown in Table 1 show high correlation coefficients between SMS-1 and NOAA-2 data in the forward scatter regions 2 and 4, with lower correlation coefficients in regions 1 and 3 where SMS-1 was monitoring forward scatter and NOAA-2 was monitoring backscatter. This discrepancy is likely explained by the presence of finite clouds and their associated scattering properties (see Figure 5) in the four regions of co-navigated data. The diurnal finite cloud curve in Figure 5 for viewing a finite cloud of the vertical ($\bar{\theta} = 18 \rightarrow 31°$) shows that an observation of a finite cloud from the sunlit side (afternoon hours

Table 1. Correlation coefficients for the four regions of simultaneous measurements by SMS-1 and NOAA-2 satellites.

Region	Correlation Coefficient
1	0.89
2	0.97
3	0.88
4	0.95

in Figure 5) will be much brighter than an observation of the same cloud viewed from the shadowed side (morning hours in Figure 5). This would explain the high correlation coefficients in regions 2 and 4 since both satellites are viewing the shadowed sides of the finite clouds resident in those regions. The correlation coefficients in regions 1 and 3 should be lower due to shape effects since SMS-1 is observing the shadowed sides of any finite clouds resident in those regions while NOAA-2 simultaneously observes the sunlit sides of those same clouds. The high correlation coefficients in regions 2 and 4 does indicate that the SMS-1 and NOAA-2 satellite data were co-navigated successfully and that the sensor response-to-count linearity assumption for both satellites is valid.

Since the correlation coefficients for areas 2 and 4 were so high (0.97 and 0.95, respectively) for the two sets of satellite data, a regression analysis was performed on the combined dataset of areas 2 and 4 to find the equation describing the relationship between the calibrated linear NOAA-2 data and the uncalibrated linearized SMS-1 data. The general form of the regression equation to be solved for is

$$c_s^{\ell} = a\, c_n^{\ell} + b \tag{3.5}$$

where c_s^{ℓ} and c_n^{ℓ} are the linearized SMS-1 and NOAA-2 counts, respectively, a is the slope and b is the y-intercept of the regression line. The slope is solved by

$$a = (\overline{c_n^{\ell} c_s^{\ell}} - \overline{c_n^{\ell}}\,\overline{c_s^{\ell}})[\overline{(c_s^{\ell})^2} - \overline{c_s^{\ell}}\,\overline{c_s^{\ell}}]^{-1}, \tag{3.6}$$

and the y-intercept is found by

$$b = \overline{c_s^{\ell}} - a\,\overline{c_n^{\ell}}\,. \tag{3.7}$$

For the combined dataset of areas 2 and 4, the slope (a) is equal to 0.683 and the y-intercept (b) has a value of 2.34.

The final calibraton equation for SMS-1 nonlinear raw count data starts with the photometric calibration equation of the NOAA-2 SR expressed by

$$N_{EFF} = 0.0067759 \frac{w}{m^2 sr} [(40c_n^{\ell}) + 20] \tag{3.8}$$

where N_{EFF} is the effective filtered radiance for the spectral response interval .515 μm $\leq \lambda \leq$ .890 μm (see Smith and Loranger (1977) for derivation). Combining Eqs. (3.3) and (3.5), a linear NOAA-2 raw count c_n^{ℓ} can be expressed in terms of a nonlinear SMS-1 raw count ($c_s^{n\ell}$) by

$$c_n^{\ell} = \frac{\left[\frac{c_s^{n\ell}}{255}\right]^2 (254.0) - 2.34}{0.683} . \tag{3.9}$$

Substituting Eq. (3.9) into Eq. (3.8) gives the final calibration equation for the nonlinear SMS-1 visible raw count data.

3.4 Calibration of SMS-1 IR Satellite Data

The IR 8-bit raw counts were converted to equivalent black temperatures (K) through the use of a standard NESS lookup table and application of appropriate calibration adjustment routines reported by Smith and Vonder Haar (1976).

3.5 Statistical Procedure Performed on Satellite Data

Cloud fields for study were selected by visually inspecting full-disc visible satellite photographs from SMS-1 and choosing 4° latitude by 1° longitude square areas to the east of the SSP (0° N, 45° W) near the equator which contained a cloud field. It is necessary to choose cloud fields to the east of the SSP and near the equator in

order to conform with the viewing geometries used in creating the theoretical satellite observations discussed in the previous chapter. The large area size was chosen so that as the cloud field was tracked during the day, the net effects of some clouds moving in and out of the area and of clouds growing and dissipating would not substantially bias the diurnal variation in observed radiance.

After calibration of the SMS-1 visible raw counts to radiances, the original 2 n. mi resolution data were reduced to 4 n. mi resolution data by averaging four adjacent values together. This averaging scheme can be thought of as a grid with a grid spacing of 4 n. mi overlaid onto the 2 n. mi resolution data and then averaging together the four 2 n. mi resolution data points that lie within each grid box. This first reduction in horizontal resolution was done to make the visible data directly comparable with the IR data which was originally 4 n. mi resolution. This allows for an assessment of the amount of cloud cover and thickness changes which could affect the diurnal variation in observed radiance.

Next, a statistical procedure was then performed on this reduced resolution visible and IR data. The first step in this procedure was to generate a frequency distribution with 30 class intervals of 3.18 radiance units for the visible data which ranges from 0 to 94.2 $Wm^{-2}sr^{-1}$ and 5 K for the IR data which ranges from 160 to 310 K. A cumulative distribution function (CDF) was then generated by summing over all of the class interval frequencies

$$CDF(x) = \frac{\sum_{i=1}^{x} n_i}{TN} , \qquad (3.10)$$

where n_i is the number of occurrences in the i^{th} class interval, TN is the total number of occurrences in all the class intervals, and x is the highest class interval in which an occurrence is found. The visible data were summed from small to large radiance values while the IR were summed from large to small values of temperature. Selected probability levels (10%, 20%, 30%, etc.) were calculated by first determining which occurrence (m) corresponds to a particular probability level by

$$m = (PL)\ (TN) \tag{3.11}$$

where PL is the probability level of interest.

Next, the class interval i in which m falls in is determined and the appropriate value (F) of radiance or temperature is computed by linearly interpolating between the endpoints of that particular class interval (i), assuming that all of the occurrences in i are evenly distributed over that class interval:

$$F = [\text{lower class interval size limit}] + \frac{m}{n_i}\ [\text{class interval size}]\ . \tag{3.12}$$

These probability levels were then plotted versus time of day to depict the variation of observed radiance and temperature during the day.

After performing the statistical procedure on both the visible and IR 4 n. mi resolution data for each hour of the day, the averaging scheme which reduced the 2 n. mi resolution data to 4 n. mi resolution data was applied to both the visible and IR 4 n. mi resolution data to reduce it to 8 n. mi resolution data. The statistical procedure described earlier was then applied to this 8 n. mi resolution data. This sequence of resolution reduction/statistical stratification was

performed for each hour of the day out to a resolution of 64 n. mi at which point the original 6400 n. mi resolution data points at 4. mi resolution were reduced to only 25 data points by the averaging scheme.

Chapter 4

DESCRIPTIVE COMPARISON OF SIMULATED DIURNAL SATELLITE OBSERVATIONS WITH SMS-1 DIURNAL SATELLITE DATA

4.1 Comparison of an Infinite Cloud Diurnal Radiance Pattern with Two Selected Cloud Fields

The simulated sequences of diurnal satellite observations for a theoretical finite and infinite cloud for selected viewing geometries show dramatic differences between the two types of clouds. A large number of cloud fields were studied in an attempt to find diurnal radiative characteristics similar to either the theoretical finite or infinite cloud. Four cloud fields were selected for a qualitative comparison with the simulated diurnal radiative behavior of the finite and infinite clouds.

4.1.1 Case 1

The first cloud field for study (Case 1) is located at 7° N latitude and 18° W longitude on July 8, 1974. The cloud field is extracted from the Intertropical Convergence Zone (ITCZ) which on this particular date is a line of large dense clouds and cloud clusters stretching across the Atlantic Ocean at 7° N latitude. Figure 11 shows that the cloud field in the Case 1 study area is composed of organized mature cumulonimbus clouds, a substantial amount of high level cirrus clouds and a variety of low and mid-level clouds situated about the cluster of thunderstorms. The areal cloud cover in the Case 1 study area is greater than 90 percent.

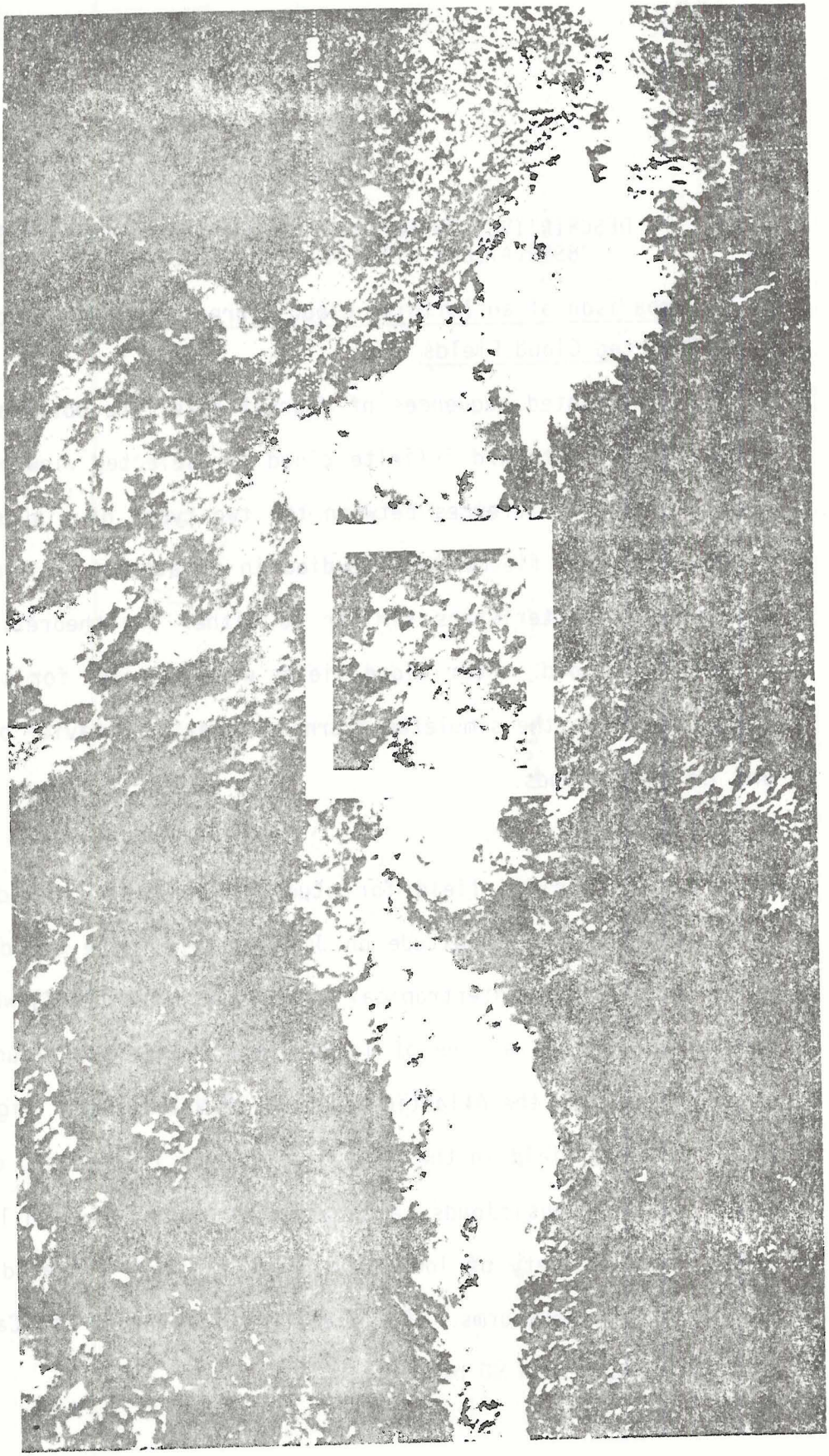

Figure 11. SMS-1 visible photograph from July 8, 1974 containing the Case 1 cloud field.

Before analyzing the visible data, the IR data is studied to determine if any major cloud changes occur that could substantially affect the diurnal character of the visible data. The diurnal variation of selected CDF probability levels for the 4 n. mi resolution IR data for Case 1 (Figure 12) reveals that two minor changes in the cloud field do occur as the day progresses. The first change is a general cooling trend in the afternoon hours which is of the greatest magnitude above the 60% probability level. The 80% and 90% probability levels cool more than 15 K between 0900 LT and 1330 LT. The second change that occurs is a slight increase in areal cloud cover (< 10 percent). This is determined by the number of data points warmer than 287 K, a threshold utilized by Smith (unpublished notes) for separating low (warm) cloud data points from background ocean data points. The 10% probability level is situated at the 286 K points at 0900 LT, and by 1430 LT is situated at the 279 K point, indicating an increase in the number of data points cooler than 287 K between those two times. The cloud scene as a whole shows a slight increase (< 5 percent) in cloud cover occurring during the late morning hours and an increase in the height of about 40 percent of the cloud cover in the afternoon hours.

The diurnal variation of radiances for 4 n. mi resolution visible data from Case 1 for selected CDF probability levels are shown in Figure 13. The probability levels from the CDF's at and above the 70% probability level exhibit a symmetry about local noon when the maximum radiances (56.0 $Wm^{-2}sr^{-1}$ at the 90 percent probability level) occur, closely resembling the theoretical diurnal variation in radiance for an infinite cloud depicted in Figure 5. The theoretical peak radiance at noon in Figure 5 is approximately 2.19 times the value of the 0800 LT

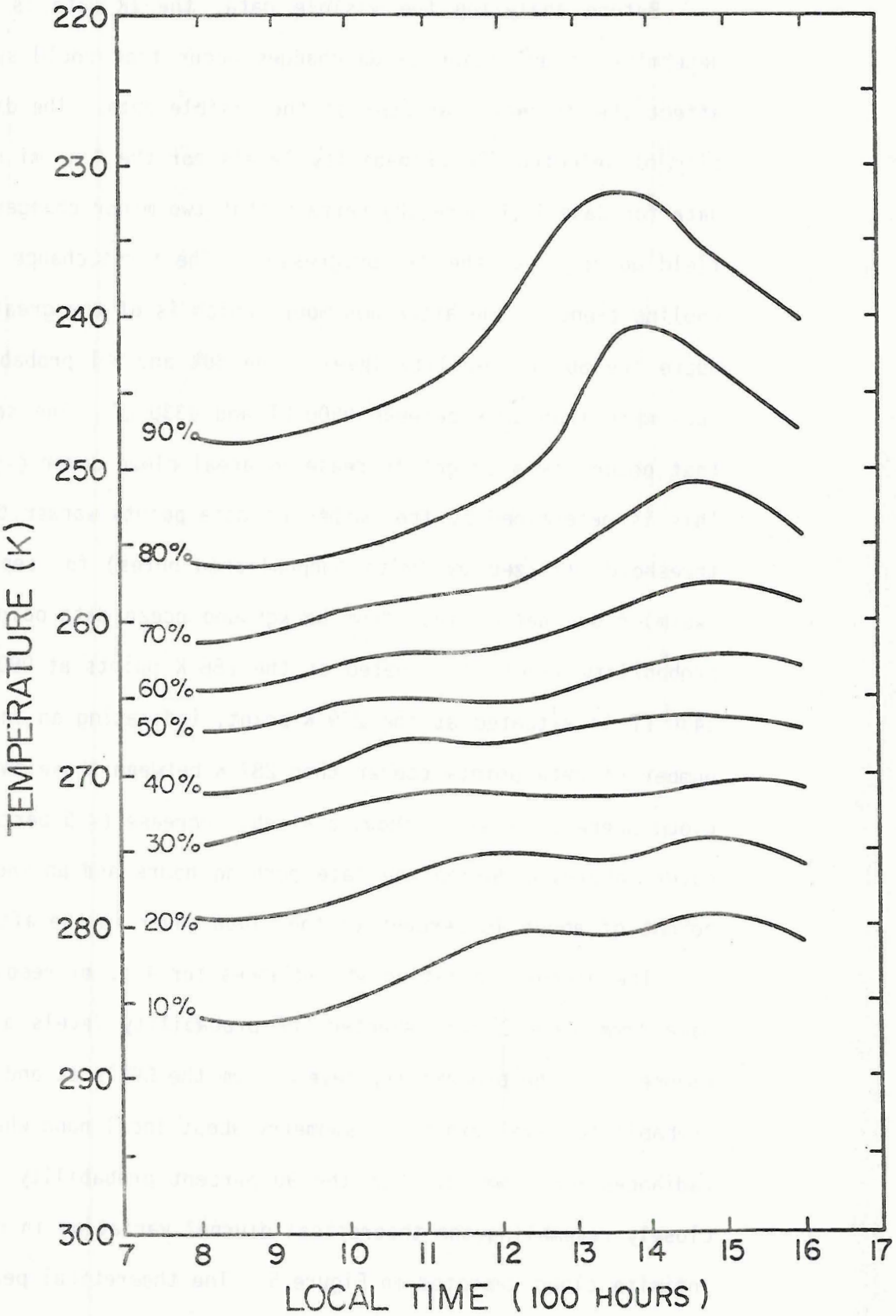

Figure 12. Diurnal variation of selected CDF probability levels for 4 n. mi resolution IR data for Case 1.

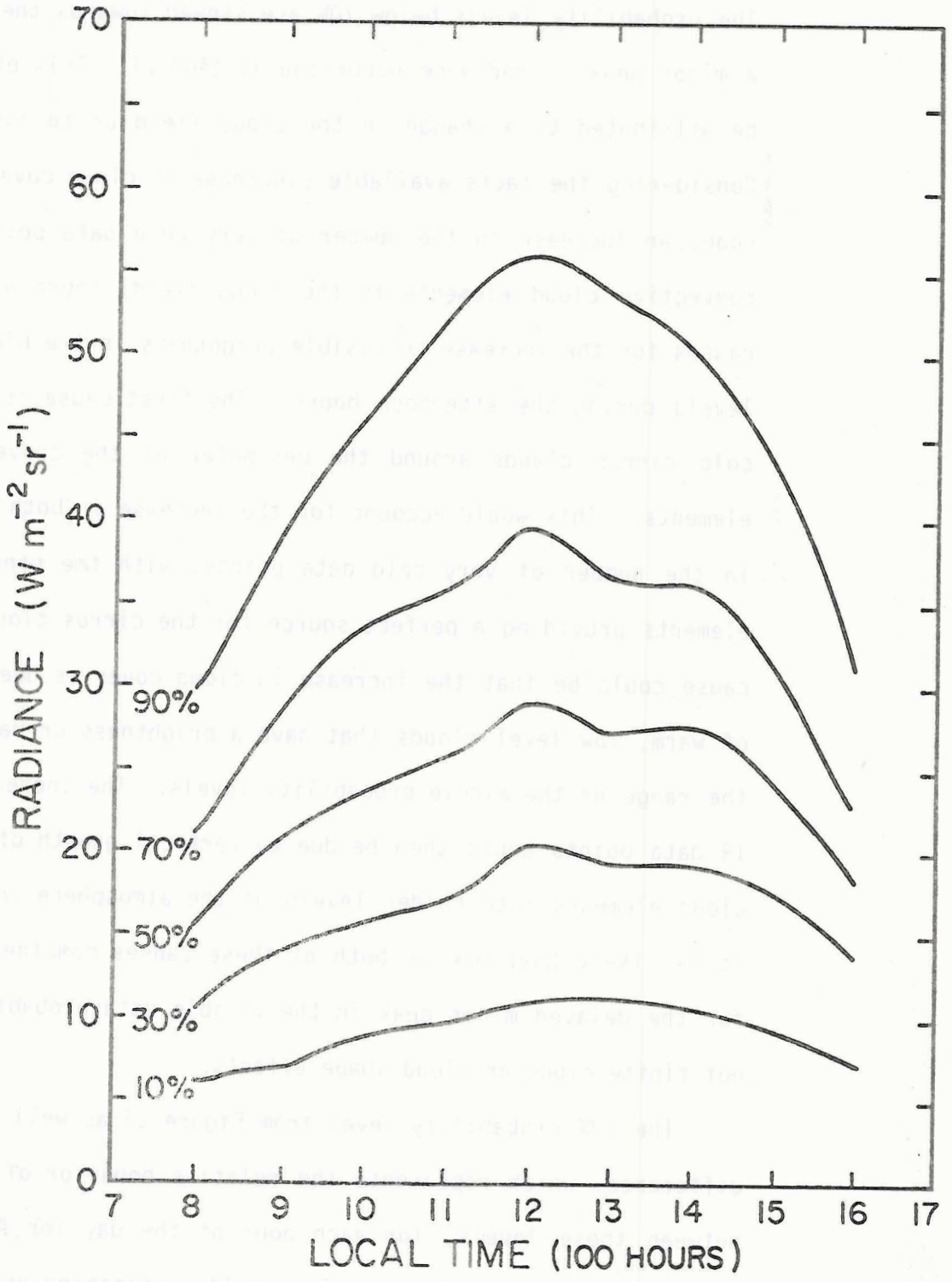

Figure 13. Diurnal variation of selected CDF probability levels for 4 n. mi resolution visible radiances for Case 1.

radiance, which is close to what is observed in Case 1 where the peak radiance at noon for the 90% level is 1.90 times the value at 0800 LT. The probability levels below 70% are skewed towards the afternoon with a minor peak in radiance occurring at 1400 LT. This phenomenon could be attributed to a change in the cloud field or to finite effects. Considering the facts available (increase in cloud cover in the afternoon, an increase in the number of very cold data points, and large convective cloud elements in the cloud field) there are two likely causes for the increase in visible brightness in the middle probability levels during the afternoon hours. The first cause is development of cold cirrus clouds around the perimeter of the convective cloud elements. This would account for the increase in both cloud cover and in the number of very cold data points, with the convective cloud elements providing a perfect source for the cirrus clouds. The second cause could be that the increase in cloud cover is due to development of warm, low level clouds that have a brightness or radiance value in the range of the middle probability levels. The increase in very cold IR data points could then be due to vertical growth of the convective cloud elements into colder levels of the atmosphere in the afternoon. It is likely that one or both of these causes combined is the reason for the delayed minor peak in the visible data probability levels and not finite cloud or cloud shape effects.

The 50% probability level from Figure 13 as well as the (90%-60%) difference, which represents the relative behavior of the data points between these levels, for each hour of the day for 4 and 16 n. mi resolution data are shown in Figure 14. Selecting probability levels were differenced in an attempt to separate the cloud data points (high

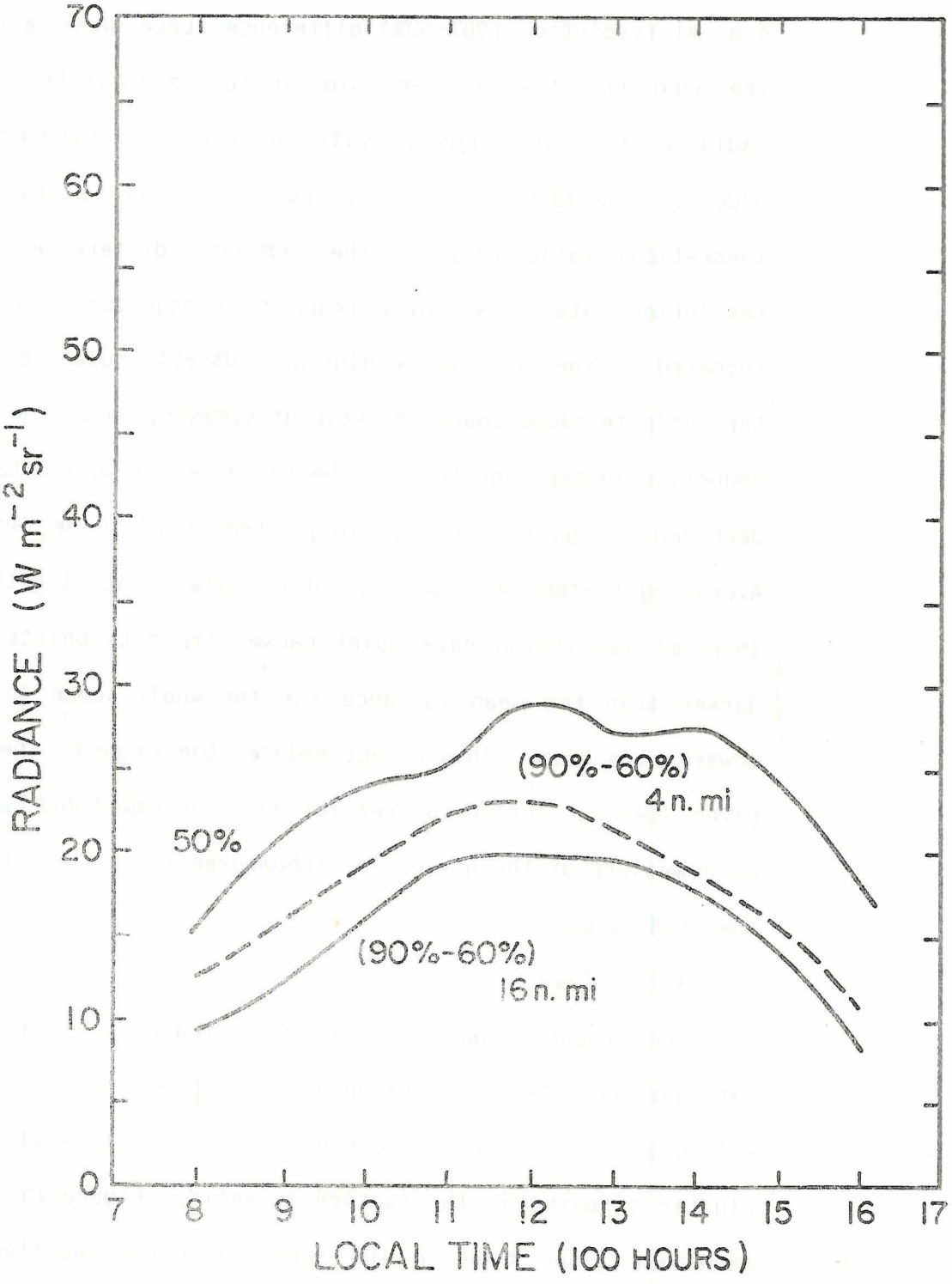

Figure 14. Diurnal variation of the 50% probability level from Figure 13 and the visible radiance (90%-60%) difference at 4 and 16 n. mi resolutions.

probabilities) from the background ocean data points (low probabilities) which are sometimes contaminated by sunglint. The 4 n. mi resolution (90%-60%) difference curve shows a symmetry about the noon hour that is very similar to the infinite cloud diurnal radiance curve in Figure 5, with the ratio of observed radiances at 0800 LT and 1200 LT (1.91) being very close to the comparable theoretical ratio (2.19). The (90%-60%) difference for 16 n. mi resolution data is slightly reduced in magnitude (~2.0 $Wm^{-2}sr^{-1}$) compared to the 4 n. mi resolution (90%-60%) curve, but still retains the infinite cloud characteristic of symmetry about the noon hour. The reduction in the magnitude of the radiances as horizontal resolution is degraded is due to the averaging scheme used to degrade resolution. Averaging sixteen 4 n. mi resolution data points together to get one 16 n. mi resolution data point causes the data points brighter and darker than the mean radiance for the whole scene to be averaged towards the mean. This effect reduces the range of the radiances in a given scene as horizontal resolution is degraded and can be considered as a measure of the horizontal inhomogeneity in the cloud field within the study area.

4.1.2 Case 2

The second cloud field for study (Case 2) is located at 5.5°N latitude and 20°W longitude on June 29, 1974. This cloud field is also extracted from the ITCZ and consists of a section of a large cloud cluster situated in the eastern Atlantic. Figure 15 shows that the prominent cloud type in the scene is cirrus outflow from the cumulonimbus clouds associated with the cloud cluster. Low and

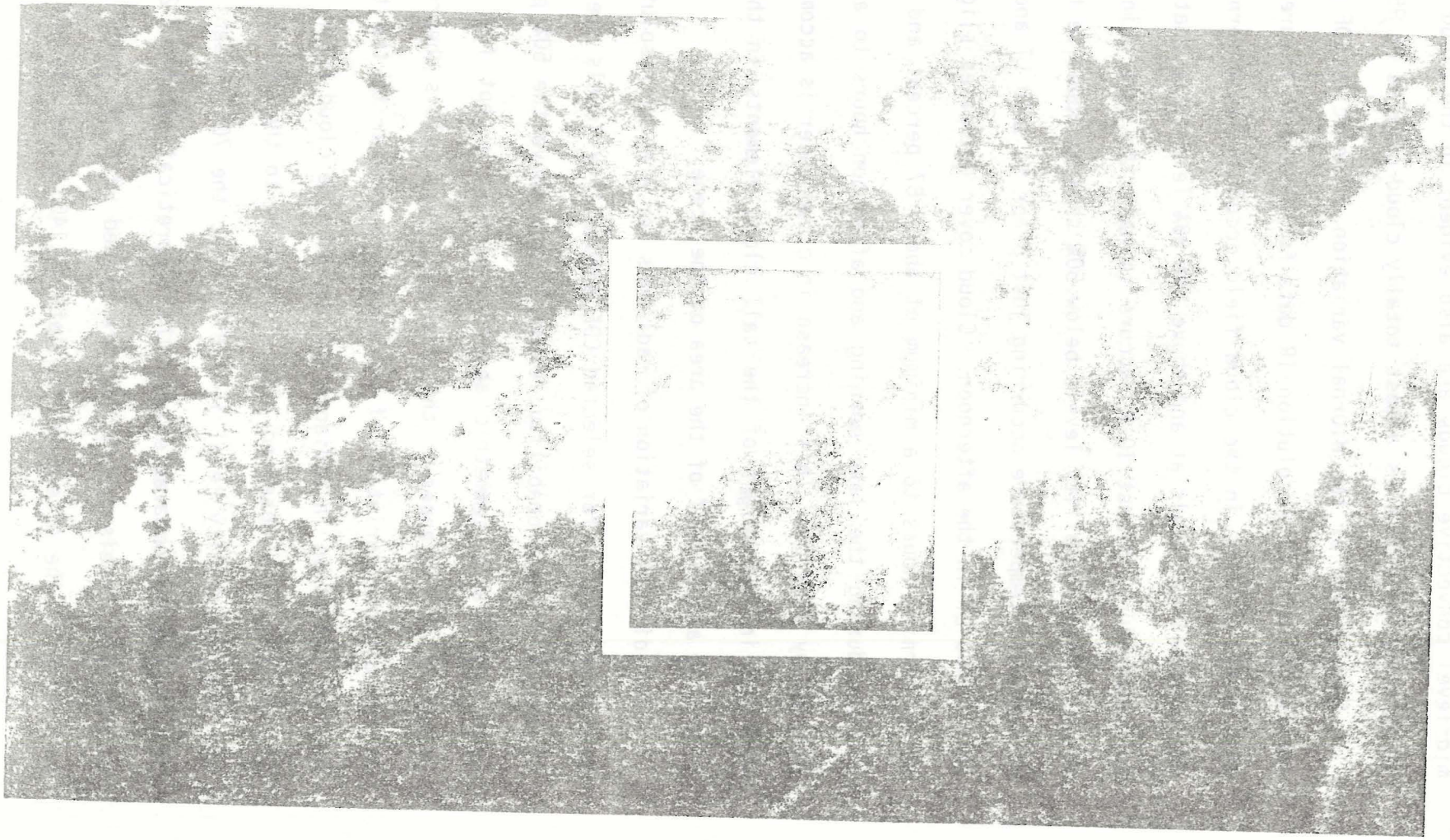

Figure 15. SMS-1 visible photograph from June 29, 1974 containing the Case 2 cloud field.

mid-level convective clouds are also evident in the cloud field. The study area in Case 2 is almost totally cloud covered (> 95 percent).

Examination of the diurnal variation of selected CDF probability levels for 4 n. mi resolution IR data for Case 2 in Figure 16 reveals that a few changes in the cloud field occur in the afternoon hours. The probability levels at and above the 50% level show that an increase in temperature, almost 10 K, occurs in half the data points in the scene. The probability levels below 50% show an opposite trend with a decrease in temperature occurring just prior to 1200 LT and continuing until 1400 LT in the afternoon. Cloud cover decreases slightly in the early morning hours to a minimum of about 87 percent and increases sharply during the late morning and afternoon hours to almost 100 percent by 1400 LT. This increase in cloud cover is accompanied by a decrease in the height of the tall cloud elements in the scene, affecting almost half of the area of the scene.

The diurnal variation of radiances for 4 n. mi resolution visible data from Case 2 for selected CDF probability levels are shown in Figure 17. The probability levels at and above the 50% probability level are nearly symmetric about local noon except for a slight reduction in radiances in the afternoon hours. This observed symmetry in the diurnal variation of radiances is similar to the theoretical diurnal variation in radiance for an infinite cloud shown in Figure 5. The ratio of the observed 1200 LT radiance to the 0800 LT radiance at the 90% probability level is 1.87 and at the 70% probability level is 1.97, both comparable with the theoretical ratio of 2.19. The probability levels below 50% are skewed with the peak radiance occurring in the afternoon, as late as 1400 LT at the 10% probability

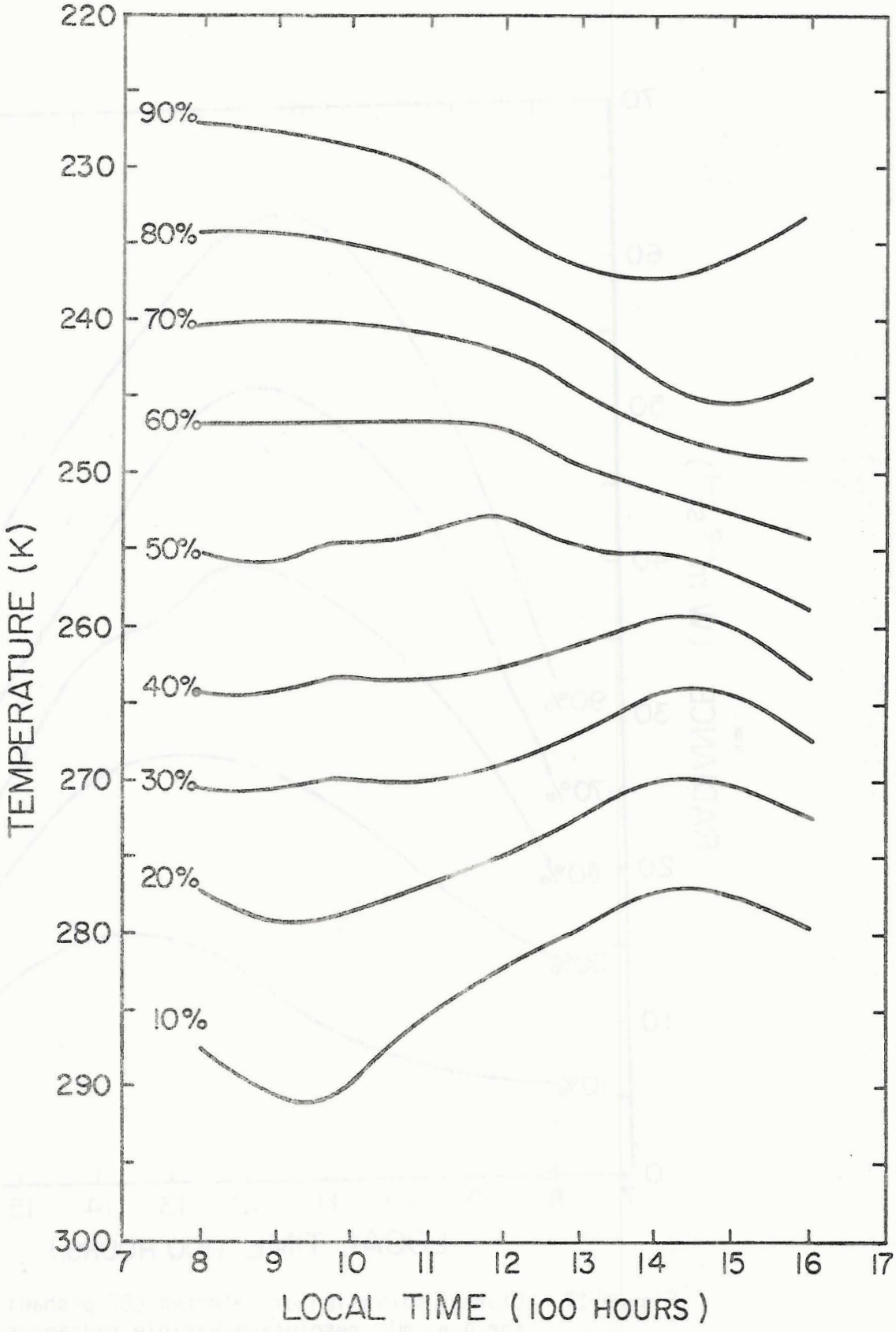

Figure 16. Diurnal variation of selected CDF probability levels for 4 n. mi resolution IR data for Case 2.

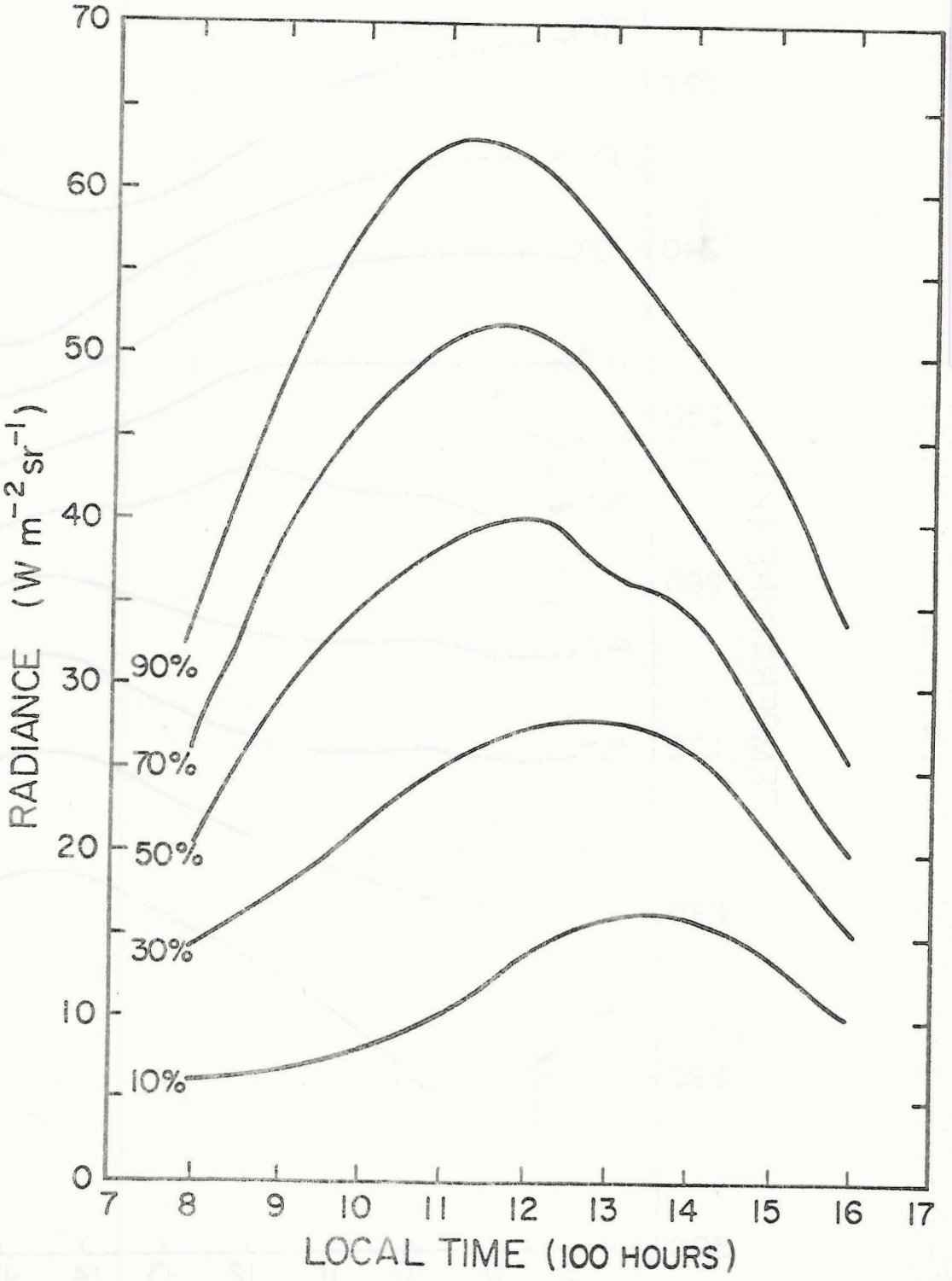

Figure 17. Diurnal variation of selected CDF probability levels for 4 n. mi resolution visible radiances for Case 2.

level. This afternoon peak in radiance, as in Case 1, is not attributed to cloud shape effects. Since the areal cloud cover is almost 100 percent, the afternoon increase in visible radiance of the lower probability levels in Figure 17 cannot be attributed to an increase in cloud cover. The probable cause for the afternoon increase in radiance is an increase in the thickness of low level warm clouds in the Case 2 study area during the afternoon, as evidenced by the cooling that occurs in the probability levels below the 50% probability level in Figure 16. The increased geometric thickness of the clouds could cause an increase in observed radiances if the cloud optical thickness increases concurrently with the geometry thickness. The converse of this argument could account for the warming of the IR high probability levels and the decrease in radiance in the visible data high probability levels. The warming trend could be associated with dissipation of the tops of dying convective towers or cirrus anvils in the cloud cluster. As these clouds dissipate, the number of very cold data points would decrease as would the number of very bright data points if this decrease in geometric thickness is accompanied by a decrease in optical thickness.

The diurnal (90%-60%) differences at 4 and 16 n. mi resolutions as well as the 50% probability level from Figure 17 for Case 2 are plotted in Figure 18. Both the 4 and 16 n. mi resolution (90%-60%) differences are skewed with the maximum value for both curves occurring at 1100 LT. This is due to the cloud field changes which caused the reduction of the afternoon radiance levels in the high probability levels in Figure 14. Even with the reduction in afternoon (90%-60%) difference

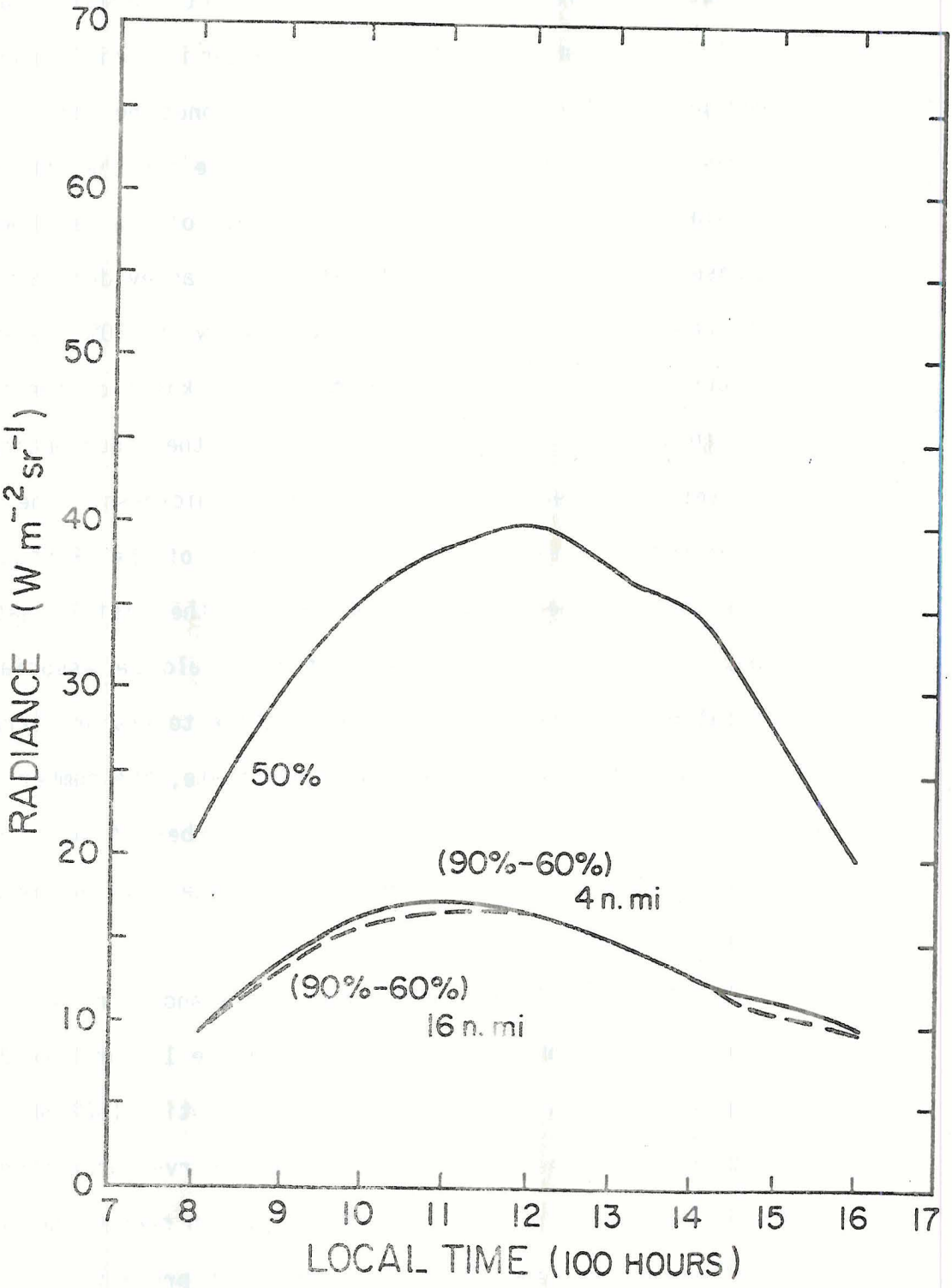

Figure 18. Diurnal variation of the 50% probability level from Figure 17 and the visible radiance (90%-60%) difference at 4 and 16 n. mi resolutions.

radiance levels, the 0800 LT to 1200 LT ratio is 1.83, very close to what was seen in Case 1 (1.91) and the theoretical infinite cloud case (2.19). This indicates that only a small amount of cloud change occurred prior to 1200 LT. The 16 n. mi resolution (90%-60%) difference is very close in magnitude to the 4 n. mi resolution (90%-60%) difference. This indicates that a higher level of horizontal homogeneity exists in the Case 2 study area than in the Case 1 study area.

4.2 Comparison of a Finite Cubic Cloud Diurnal Radiance Pattern with Two Selected Cloud Fields

4.2.1 Case 3

The third cloud field for study (Case 3) is located at 0°N latitude and 33°W longitude on July 8, 1974. Figure 19 shows that this is a broken cloud field consisting of low and mid-level clouds and cloud groups ranging in size up to 50 n. mi in diameter. There is no apparent cloud field organization to this particular cloud field except for the clumping of clouds together into cloud groups. The Case 3 study area has about 20 to 25 percent of its 4° latitude by 4° longitude area covered by clouds.

Examination of the diurnal variation of selected CDF probability levels for 4 n. mi resolution IR data for Case 3 (Figure 20) reveals that some minor changes in the cloud field are occurring during the day, but these changes are working in opposition to any finite cloud effects that may be occurring during the day. The first change is a warming that is occurring at the 90%, 80% and 70% probability levels. The 90% level warms from 272 K at 0800 LT to 281 K at 1300 LT which is then followed by a slight cooling trend to 277 K by 1600 LT. This

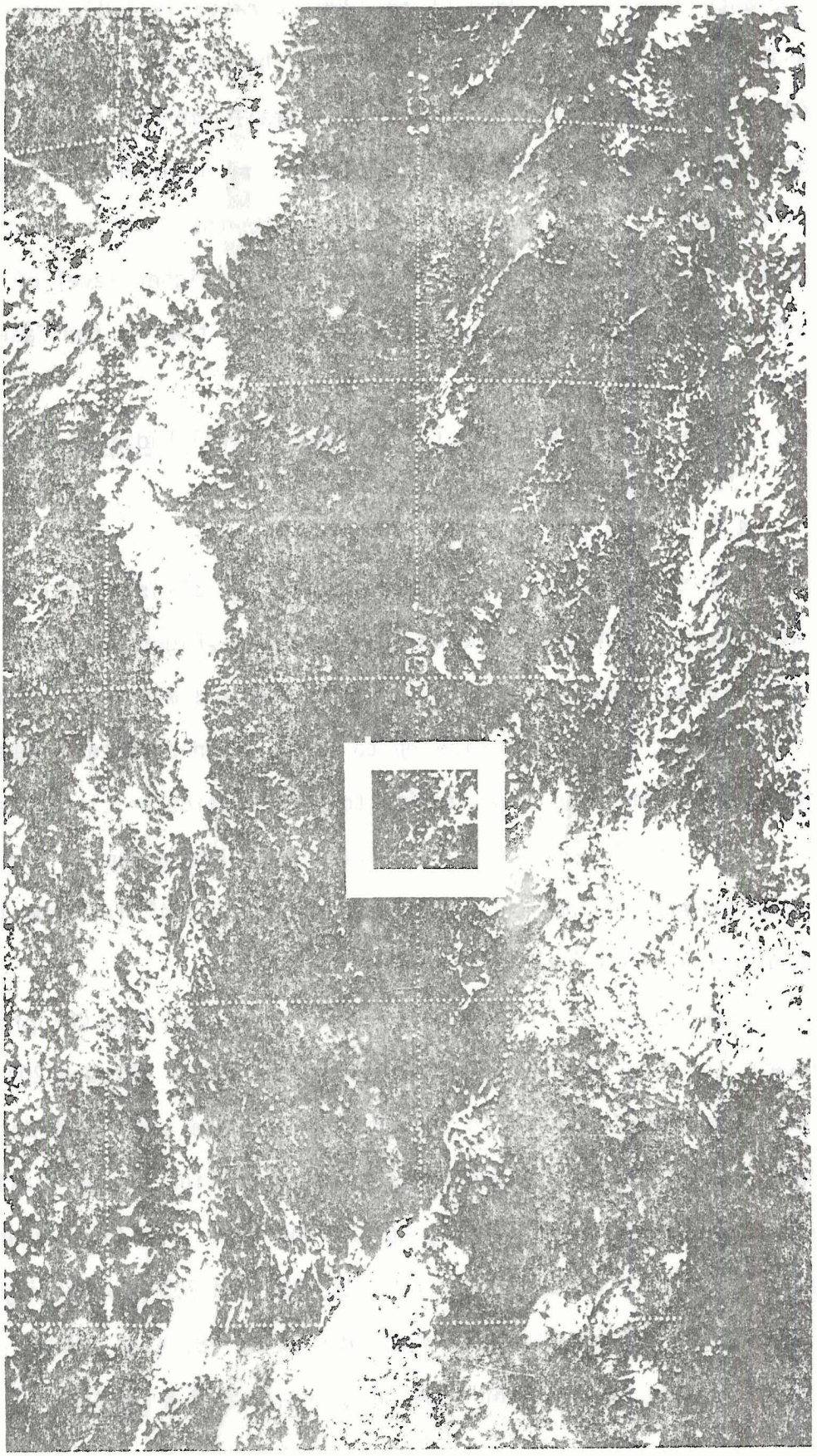

Figure 19. SMS-1 visible photograph from July 8, 1974 containing the Case 3 cloud field.

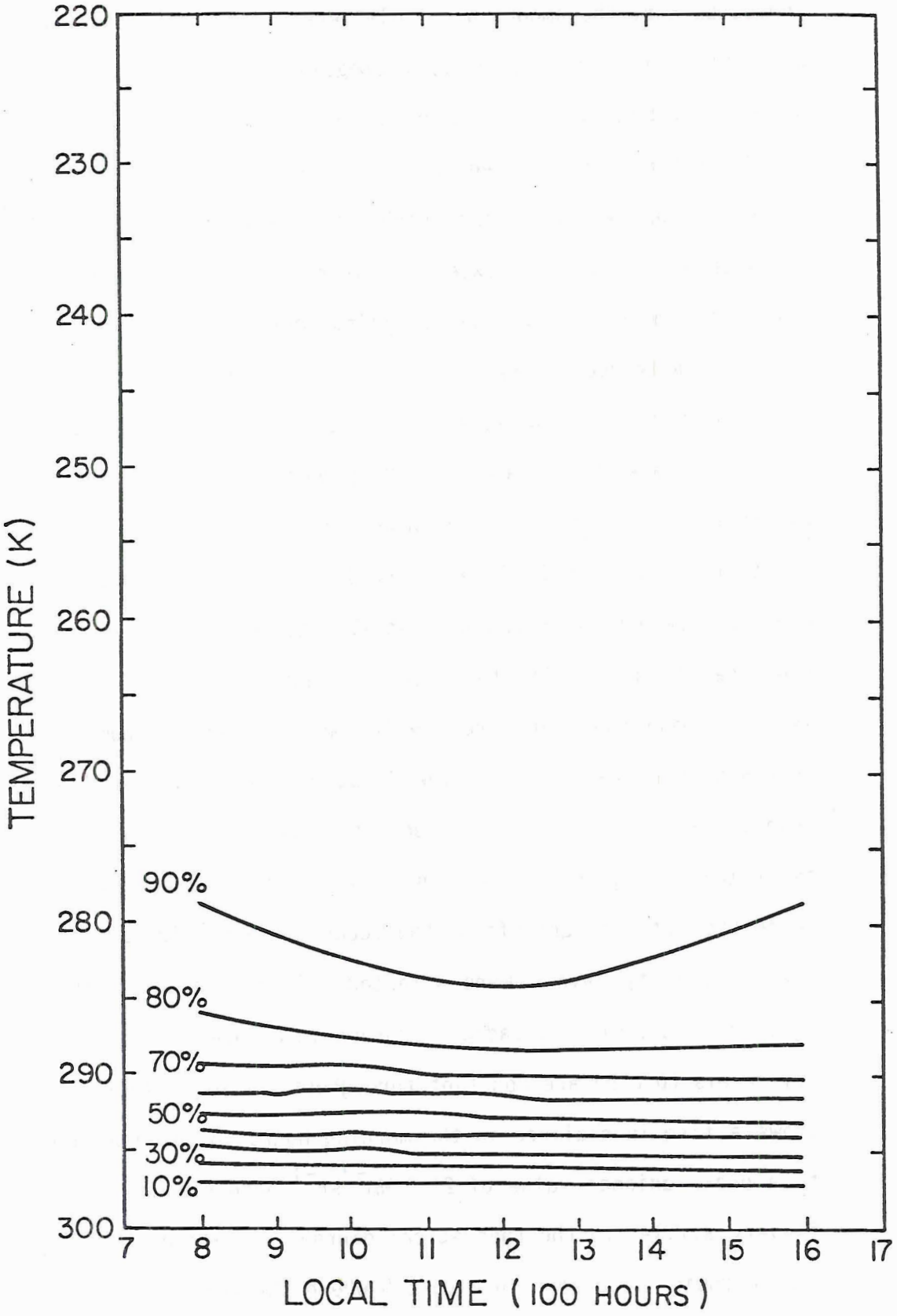

Figure 20. Diurnal variation of selected CDF probability levels for 4 n. mi resolution IR data for Case 3.

indicates that the amount of middle level cloudiness during the morning and early afternoon hours is decreasing. This warming trend is accompanied by about a 6 percent decrease in total cloud cover based on the 287 K threshold. Based solely on the knowledge that cloud cover is decreasing as well as cloud height, the expected diurnal variation in radiance would have the expected maximum radiance occurring sometime during the morning hours and a minimum observed radiance occurring in the early afternoon hours.

The diurnal variation of radiances for 4 n. mi resolution visible data from Case 3 for selected CDF probability levels are shown in Figure 21. Instead of the diurnal radiance curves being symmetric about local noon as in Cases 1 and 2, all of the probability levels plotted show a peak in radiance at 1130 LT followed by a second peak in radiance at 1400 LT for the levels at and above the 70% probability level. These two peaks are due to two different phenomena and are independent of each other. The first peak (21.0 $Wm^{-2}sr^{-1}$ at the 90% level) that occurs in all probability levels is due to sunglint which is contaminating the cloud scene. Sunglint is caused by the specular reflection of sunlight off of the ocean surface which explains why the low probability levels were affected. If the sunlight effects are ignored in the diurnal radiance curves in Figure 21, the low probability levels (ocean) are constant throughout the day, while the 90% level shows a rise in radiance in the morning hours followed by a rapid rise to a peak radiance value of 21.0 $Wm^{-2}sr^{-1}$ occurring at 1400 LT. This is very similar to the theoretical diurnal variation of radiance for a finite cubic cloud seen in Figure 5 where the theoretical peak radiance also occurs at 1330 LT. The 1330 LT theoretical radiance is 42 percent

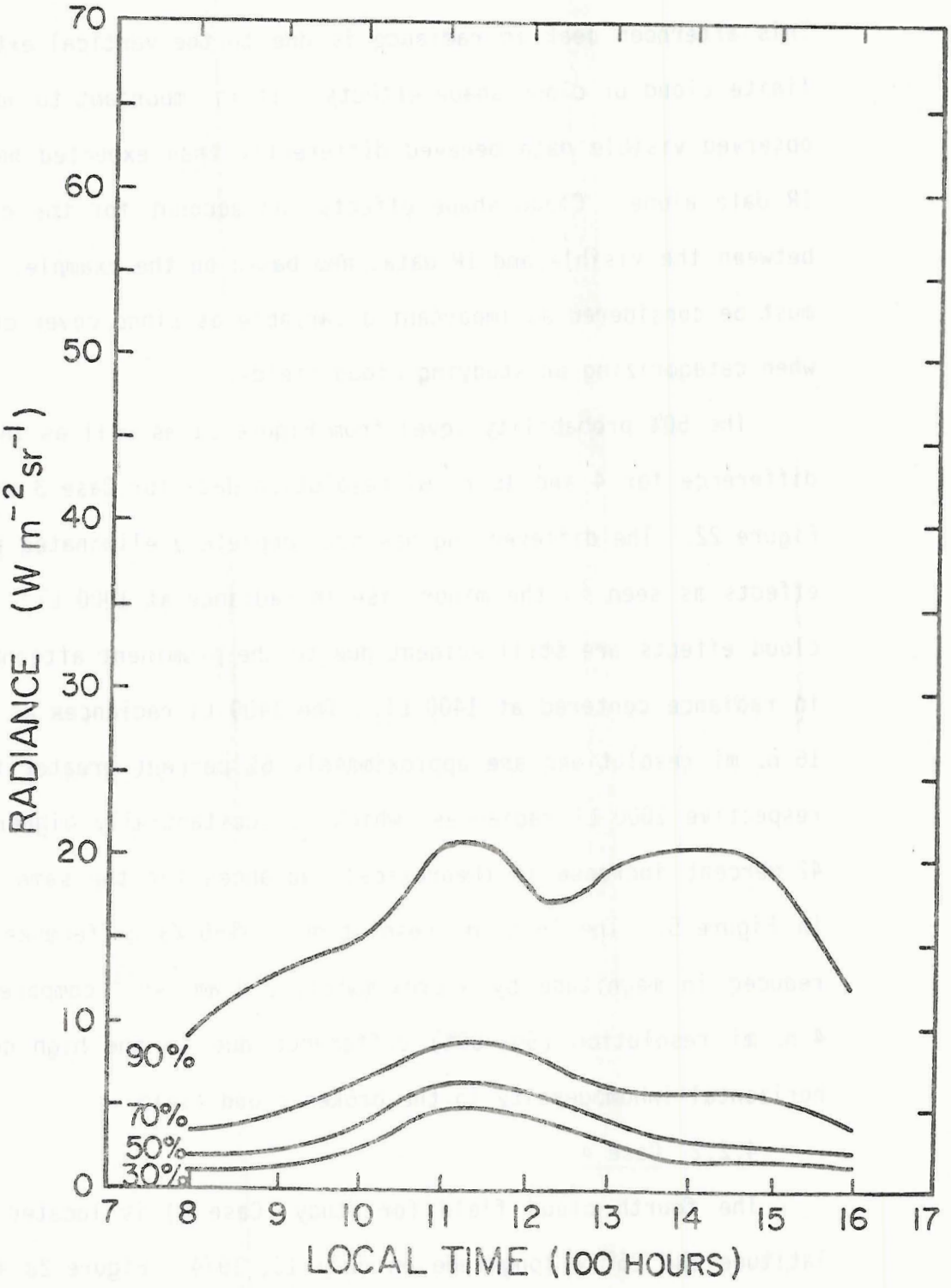

Figure 21. Diurnal variation of selected CDF probability levels for 4 n. mi resolution visible radiances for Case 3.

greater than the 1000 LT radiance which is very close to the 40 percent increase in observed radiance seen in Case 3 for the same two times. This afternoon peak in radiance is due to the vertical extent of the finite cloud or cloud shape effects. It is important to note that the observed visible data behaved differently than expected based on the IR data alone. Cloud shape effects can account for the discrepancy between the visible and IR data, and based on the example, cloud shape must be considered as important a variable as cloud cover and thickness when categorizing or studying cloud fields.

The 50% probability level from Figure 21 as well as the (90%-60%) difference for 4 and 16 n. mi resolution data for Case 3 are shown in Figure 22. The differencing has not completely eliminated the sunglint effects as seen in the minor rise in radiance at 1000 LT. The finite cloud effects are still evident due to the prominent afternoon maximum in radiance centered at 1400 LT. The 1400 LT radiances at both 4 and 16 n. mi resolutions are approximately 61 percent greater than their respective 1000 LT radiances, which is substantially higher than the 42 percent increase in theoretical radiances for the same two times in Figure 5. The 16 n. mi resolution (90%-60%) difference curve is reduced in magnitude by approximately 2.0 $Wm^{-2}sr^{-1}$ compared to the 4 n. mi resolution (90%-60%) difference due to the high degree of horizontal inhomogeneity in the broken cloud field.

4.2.2 Case 4

The fourth cloud field for study (Case 4) is located at 2° S latitude and 25° W longitude on July 13, 1974. Figure 23 shows that this is a broken cloud field consisting of low-level clouds and cloud groups that range in size up to 40 n. mi in diameter. Some cloud field

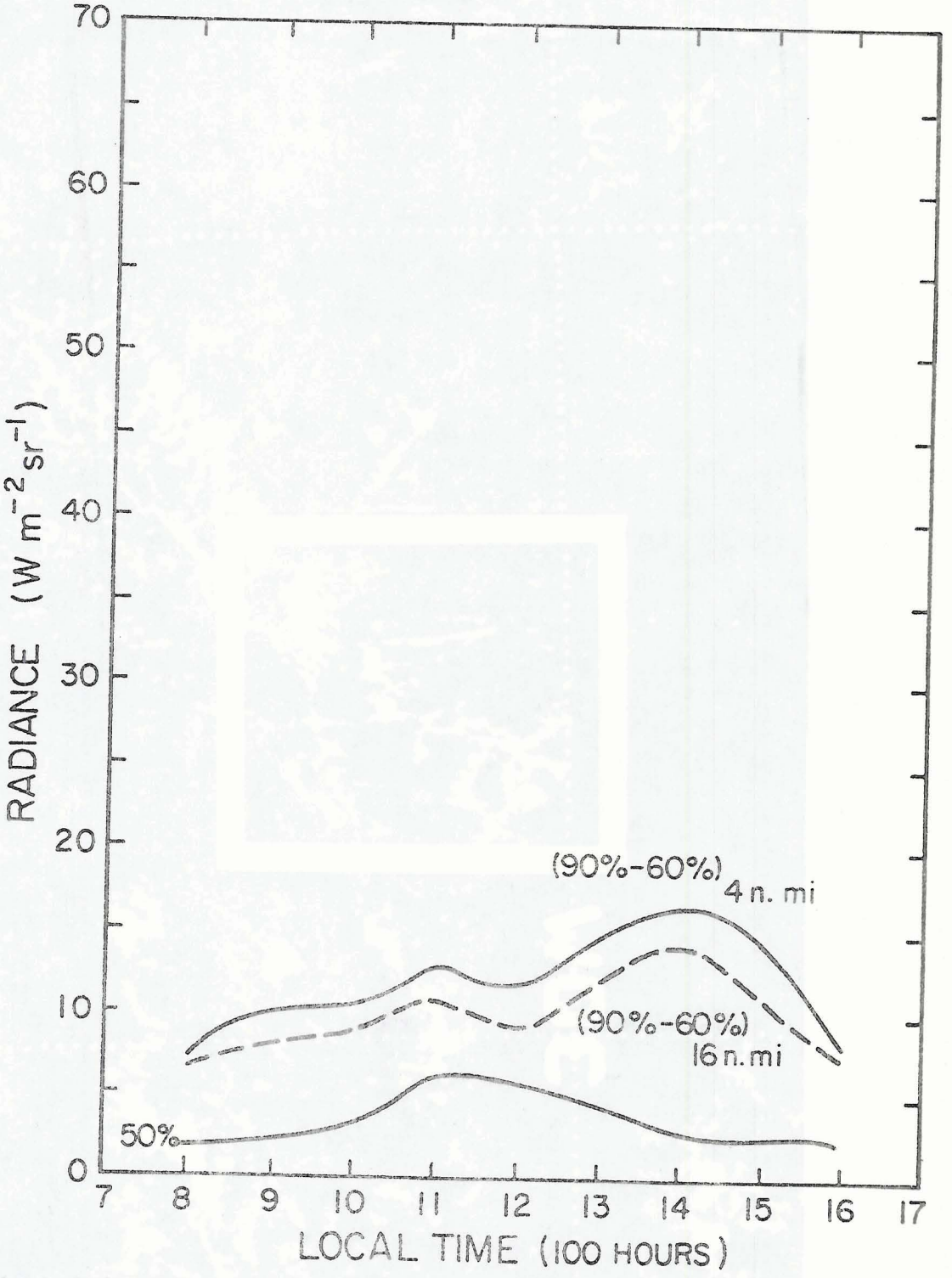

Figure 22. Diurnal variation of the 50% probability level from Figure 21 and the visible radiance (90%-60%) difference at 4 and 16 n. mi resolutions.

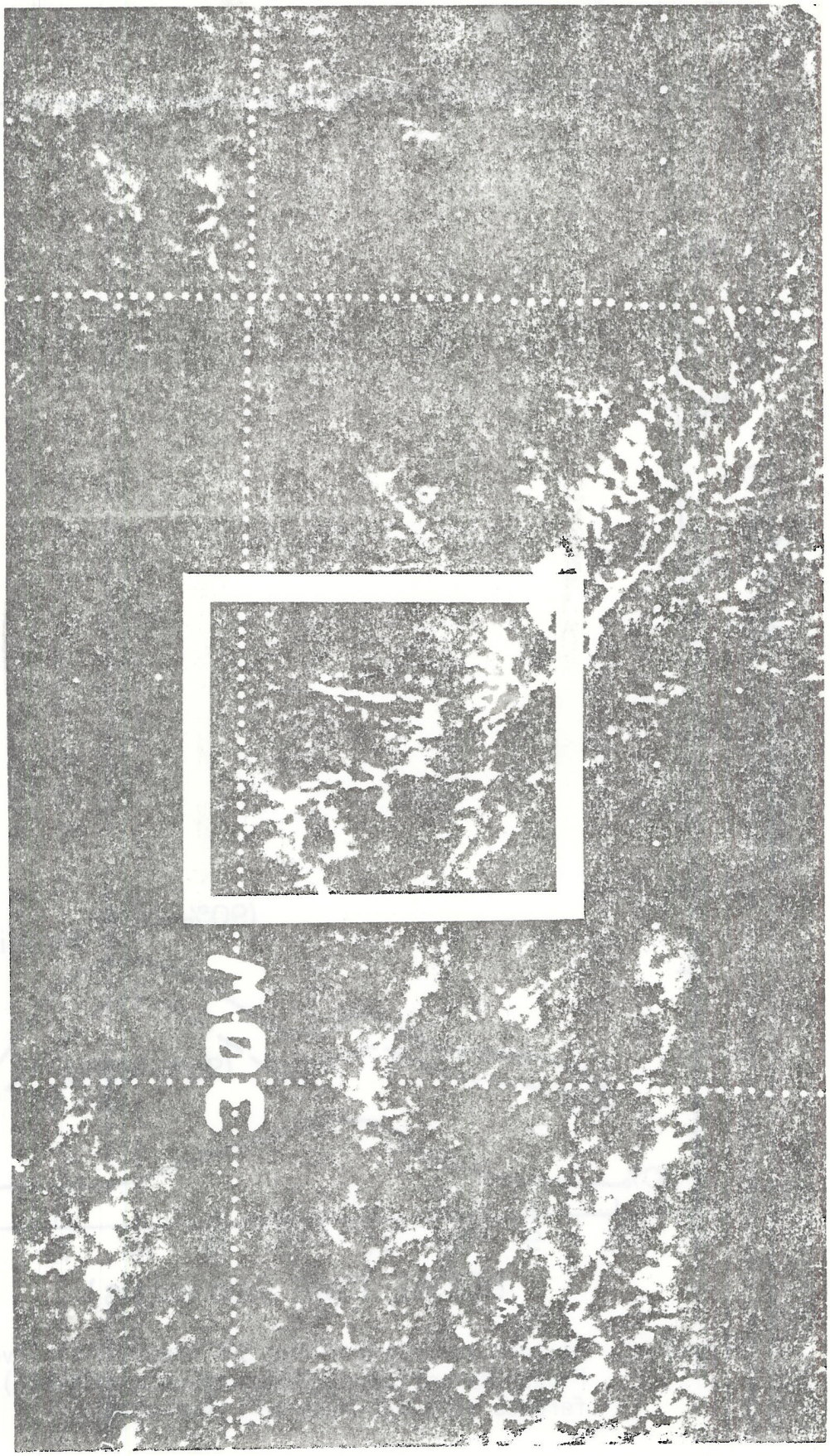

Figure 23. SMS-1 visible photograph from July 13, 1974 containing the Case 4 cloud field.

organization is evident in the cloud scene with the majority of clouds and cloud groups running diagonally through the center of the 4° latitude by 4° longitude study area, extending from the northwest corner all the way to the southeast corner. This main band of clouds is accompanied by a number of smaller bands of clouds to the southwest and parallel to the main band. The clouds cover about 25 percent of the Case 4 study area.

The diurnal variation of selected CDF probability levels for 4 n. mi resolution IR data for Case 4 are shown in Figure 24. Since the visible data shows that almost 25 percent of the study area is cloud covered and all of these clouds are warm low clouds, a threshold temperature of 288 K is more appropriate for separating cloud and ocean data points than the 287 K threshold used in Cases 1, 2, and 3. Overall, Figure 24 shows little change occurring in the cloud field during the day. No change in cloud cover occurs, a very slight cooling of the 90% probability level occurs in the afternoon, and a slight cooling occurs in the ocean values (10% level) during the day.

The diurnal variation of radiances for 4 n. mi resolution visible data from Case 4 for selected CDF probability levels are shown in Figure 25. The 1100 LT data were not available for analysis and were estimated by interpolating between the 1000 and 1200 LT data. This estimated data is actually a better representation of what would be observed at 1100 LT since the observed data would have been contaminated with sunglint in a manner similar to Case 3 (Figure 21). The probability levels at and above the 70% level are skewed with a maximum radiance of 20.0 $Wm^{-2}sr^{-1}$ at the 90% level occurring at 1400 LT. This is very similar to the diurnal variation of radiances

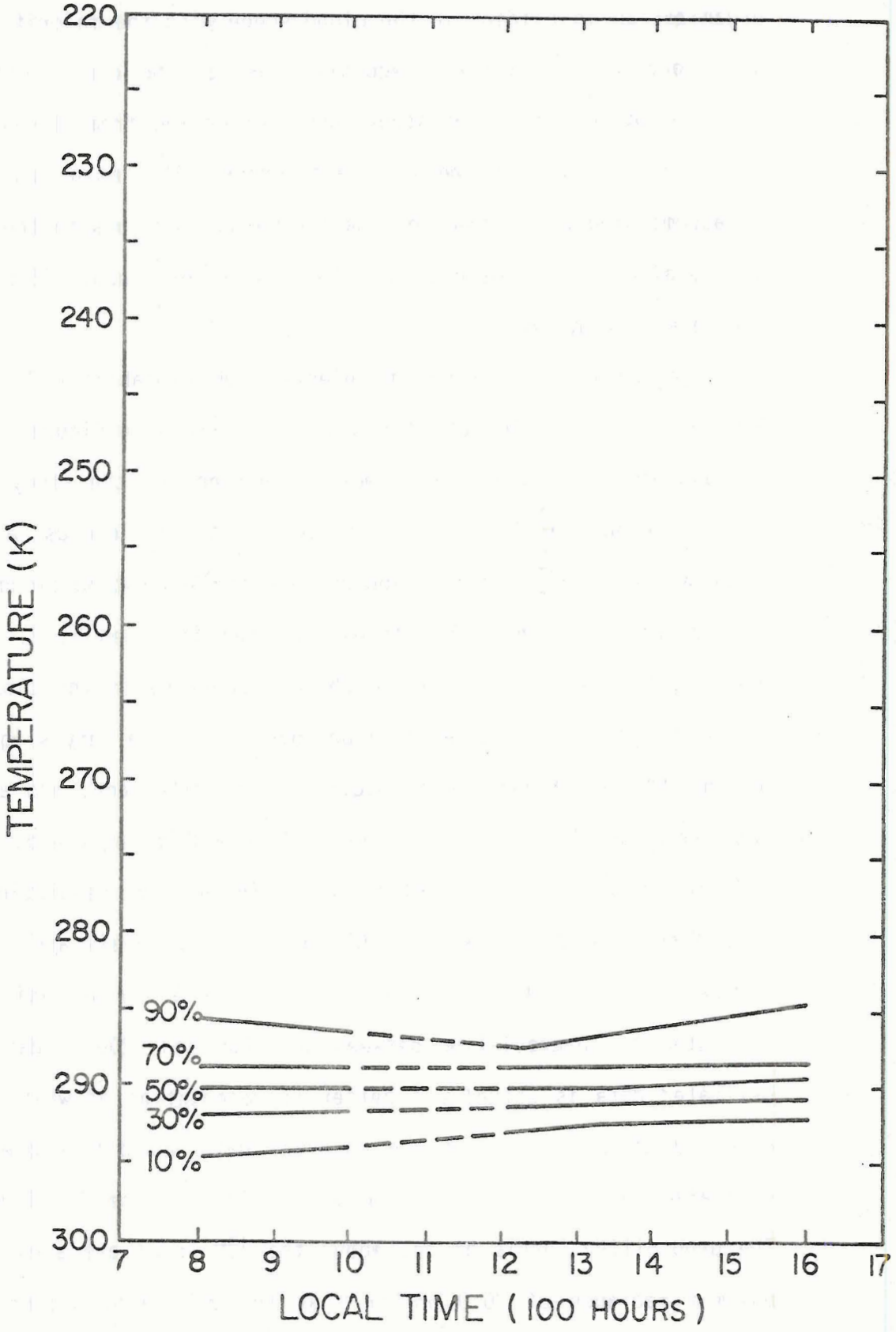

Figure 24. Diurnal variation of selected CDF probability levels for 4 n. mi resolution IR data for Case 4.

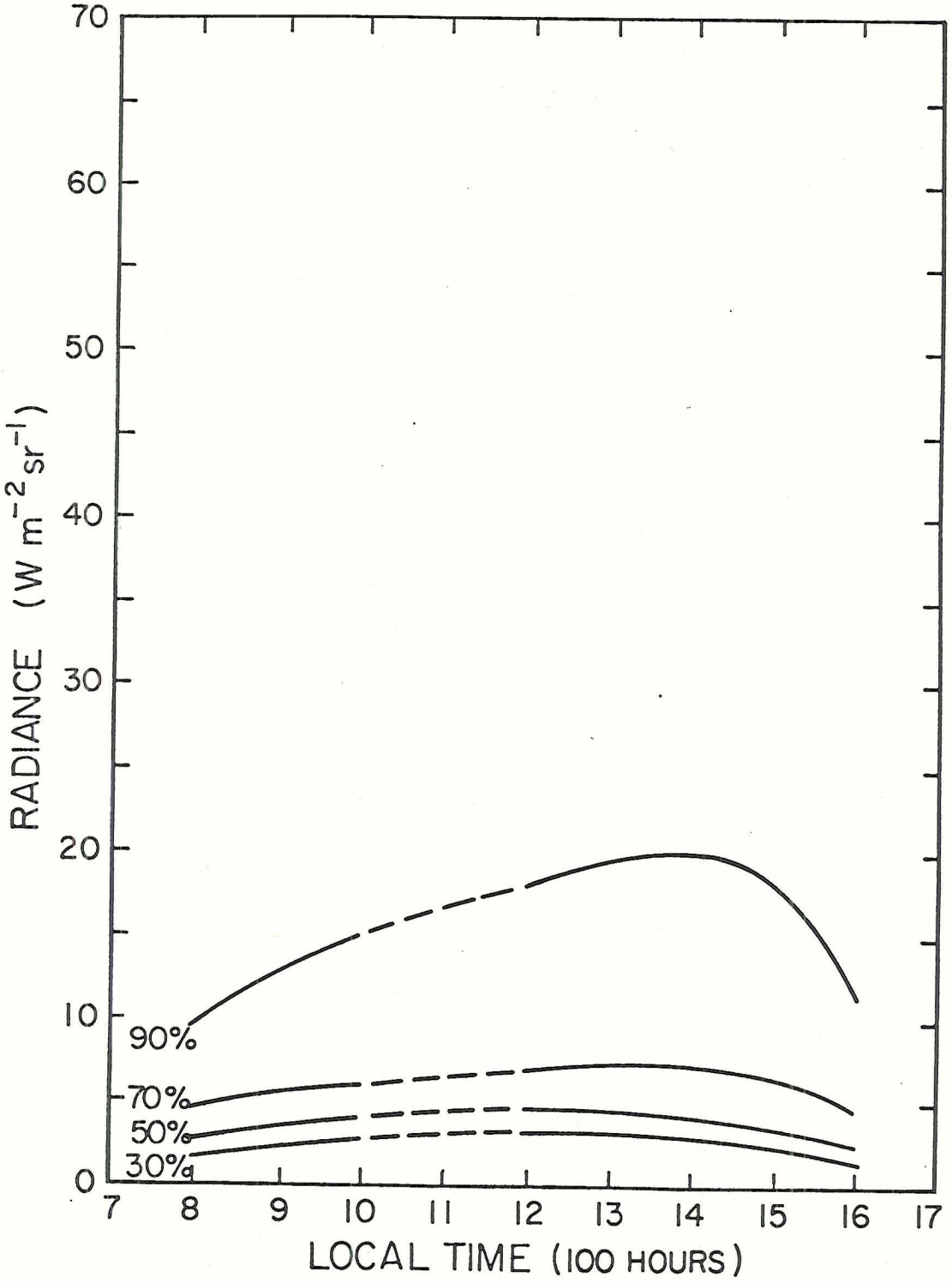

Figure 25. Diurnal variation of selected CDF probability levels for 4 n. mi resolution visible radiances for Case 4.

seen for the finite cloud (Figure 5) and in Case 3 (Figure 21). The 1330 LT radiance is 33 percent greater than the 1000 LT radiance comparable to the 42 percent and 40 percent increases seen in the theoretical finite cloud case and Case 3, respectively, for the same two times. The 50% and 30% probability levels show little change during the day, with some sunglint effects evident from 0900 LT to 1300 LT. Since the IR data showed that no large change in the cloud field occurs during the day, the afternoon maximum radiance observed in the high probability levels in Figure 25 is due to cloud shape effects.

The 50% probability level from Figure 25 as well as the (90%-60%) difference at 4 and 16 n. mi resolution for Case 4 are shown in Figure 26. The finite cloud effects are still evident due to the prominent afternoon maximum in radiance at 1400 LT. The 1400 LT radiances at both 4 and 16 n. mi resolutions are approximately 68 percent greater than their respective 1000 LT radiances. This is comparable to the 61 percent increase in theoretical finite cloud radiance for the same two times in Figure 5. The 16 n. mi resolution (90%-60%) difference curve is reduced in magnitude by at least 2.0 $Wm^{-2}sr^{-1}$ compared to the 4 n. mi resolution (90%-60%) difference. This is comparable to the amount of reduction seen in Cases 1 and 3 and is representative of a high degree of horizontal inhomogeneity.

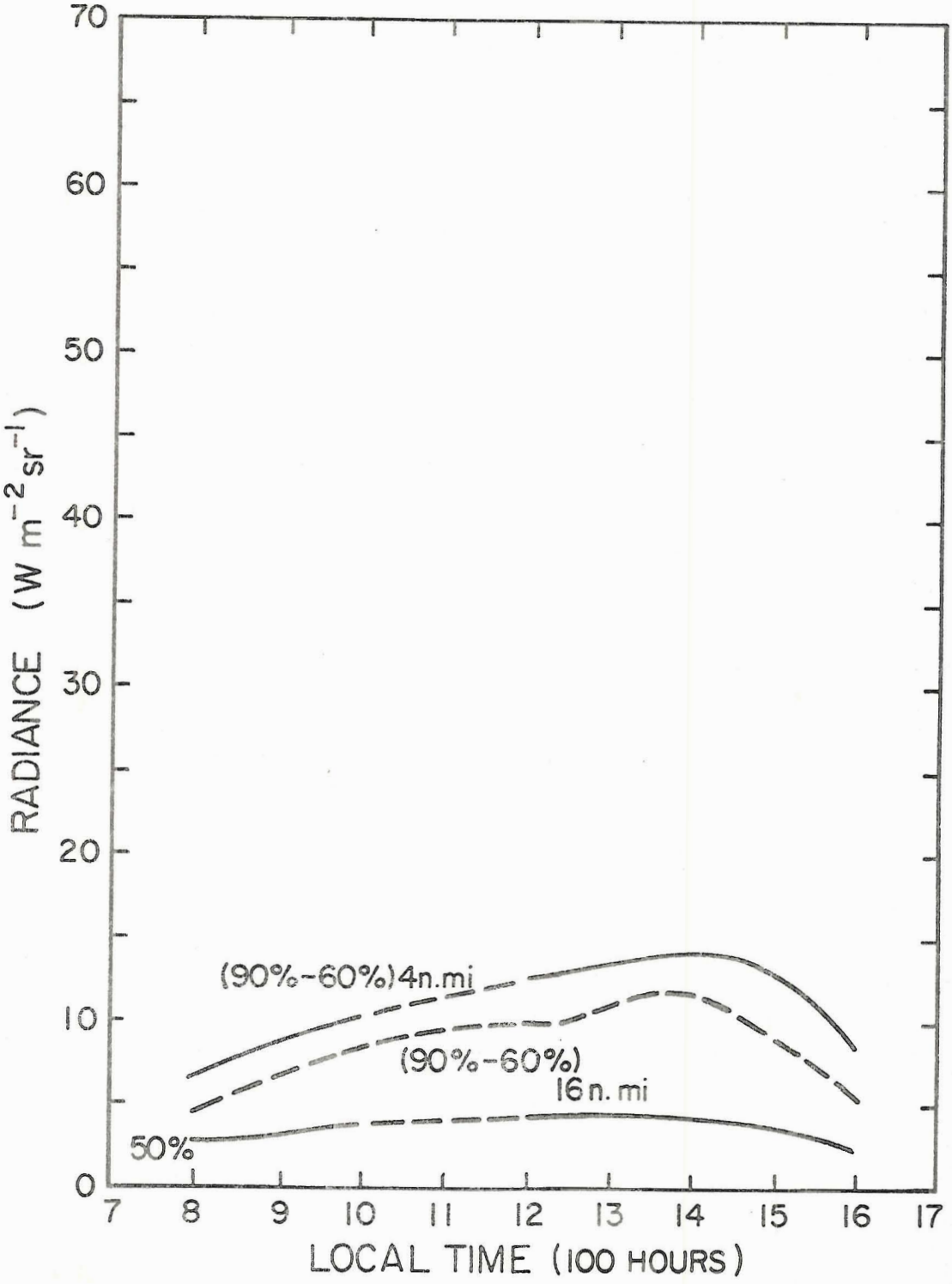

Figure 26. Diurnal variation of the 50% probability level from Figure 25 and the visible radiance (90%-60%) difference at 4 and 16 n. mi resolutions.

Chapter 5

SUMMARY AND CONCLUSIONS

The effects of finite and semi-infinite cloud shape on diurnal satellite observations were investigated by simulating diurnal satellite observations of a finite cubic and semi-infinite cloud and comparing these results with actual satellite observations of cloud fields with cloud cover varying from less than 30 percent to greater than 90 percent.

Theoretical satellite observations were created by computing relative radiances from a theoretical model which used the Monte Carlo method to simulate the scattering of solar radiation by a finite cubic and infinite cloud for optical depths of 73.5 and 20.0. These radiances were computed for five different solar illumination angle and then adjusted to simulate a series of geostationary satellite observations during the day. These computations were made with the satellite and clouds situated in the equatorial plane at the equinox. The diurnal variations in radiance for a theoretical infinite and finite cubic cloud viewed at a zenith viewing angle (θ) of 0° were both symmetric about local noon when the maximum radiance occurred. This was true for both optical depths. When viewing the same clouds from an average zenith viewing angle of 18 to 31° (measured westward from zenith) the diurnal variation in radiance for the infinite cloud was again essentially symmetric about local noon when the maximum radiance occurred. The finite cubic cloud, however, had a skewed

diurnal variation in radiance with the maximum radiance occurring at 1400 local time. This was true for both optical depths.

The diurnal variation in radiance for the infinite and finite clouds were then compared to diurnal radiance data from cloud fields observed by geostationary satellite (SMS-1). The comparison was accomplished by forming frequency distributions for each hour of digitized visible satellite data for a cloud scene and then generating cumulative distribution functions (CDF) from those hourly frequency distributions. Selected CDF probability levels from each hour were plotted as a function of time and the compared to the theoretical diurnal variation of radiance.

Two cloud fields consisting of cloud clusters that covered more than 90 percent of the 4° latitude by 4° longitude study area were chosen to examine the diurnal radiance pattern of semi-infinite clouds. The observed radiance pattern for both of the observed cloud fields closely resembled the theoretical radiance pattern for an infinite cloud with the pattern being symmetric about local noon when the maximum radiance occurred. This was true for both the probability levels at and above the 70% level and the (90%-60%) differences at 4 and 16 n. mi resolutions for both cases.

Two cloud fields consisting of scattered clouds that covered less than 30 percent of the study areas were chosen to examine the diurnal radiance pattern of finite clouds. The 90% probability levels as well as the (90%-60%) differences at 4 and 16 n. mi resolutions for both observed cloud fields closely resembled the theoretical radiance pattern for a finite cloud viewed from $\bar{\theta} = 18 \rightarrow 31°$, with the greater radiances occurring during the afternoon hours and peaking at 1400 LT.

The results from the four cloud fields show that the radiative features of semi-infinite and finite clouds can both be found in satellite observations. This was true not only for the high resolution data (4 n. mi), but also for 16 n. mi resolution data which indicates that none of these cloud radiative features are resolution dependent. These results mean that care should be used in interpreting and using satellite data since cloud shape and the viewer, cloud and solar geometry can significantly influence the magnitude of the observed radiances.

REFERENCES

Aida, Masaru, 1977: Scattering of solar radiation as a function of cloud dimensions and orientation. J. Quant. Spectrosc. Radiat. Transfer, 17, pp. 303-310.

Avaste, O. A. and G. M. Vainikko, 1976: A method of calculating radiative transfer in broken clouds. Paper presented at Symposium of Radiation in the Atmosphere, Garmisch-Partenkirchen, Germany, held 19-28 August 1976.

Barkstrom, B. R. and R. F. Arduine, 1976: The effect of finite horizontal size of clouds upon the visual albedo of the earth. Paper presented at Symposium of Radiation in the Atmosphere, Garmisch-Partenkirchen, Germany, held 19-28 August 1976.

Busygin, V. P., N. A. Yevstratov and Ye. M. Feygelśon, 1973: Optical properties of cumulus and radiant fluxes for cumulus cloud cover. Atmos. Oceanic Phys., 9, pp. 1142-1151.

Cashwell, E. D. and C. J. Everett, 1959: A Practical Manual on the Monte Carlo Method for Random Walk Problems. Pergamon Press, 153 p.

Danielson, R. E., D. R. Moore, and H. C. Van de Hulst, 1969: The transfer of visible radiation through clouds. J. Atmos. Sci., 26, pp. 1078-1087.

Davies, R. and J. A. Weinman, 1976: Results from two models of the three dimensional transfer of solar radiation in finite clouds. Paper presented at Symposium of Radiation in the Atmosphere, Garmisch-Partenkirchen, Germany, held 19-28 August 1976.

Davies, R., 1978: The effect of finite geometry on the three-dimensional transfer of solar irradiance in clouds. J. Atmos. Sci., 35, pp. 1712-1725.

Davis, John M., Stephen K. Cox, and Thomas B. McKee, 1978: Solar absorption in clouds of finite horizontal extent. Paper presented at Third Conference on Atmospheric Radiation, Davis, California, held 28-30 June 1978.

Deirmendjian, D., 1969: Electromagnetic Scattering on Spherical Polydispersions. American Elsevier, 290 p.

DeMaria, M. and T. B. McKee, 1979: A comparison of theoretical and observed radiances from non-precipitating cumulus clouds. Atmospheric Science Paper #313, Colorado State University.

Ellis, J. S. and T. H. Vonder Haar, 1976: Zonal average earth radiation budget measurements from satellites for climate studies. Atmospheric Science Paper #240, Colorado State University.

Gautier, C., G. Diak, and S. Masse, 1980: A simple physical model to estimate incident solar radiation at the surface from GOES satellite data. Journal of Applied Meteorology, 19, pp. 1005-1012.

Jacobowitz, H., W. L. Smith, H. B. Howell, F. W. Nagle, and J. R. Hickey, 1977: The first eighteen months of planetary radiation budget measurements from the Nimbus 6 ERB experiments (submitted to Bull. Amer. Meteor. Soc.).

Jones, G. D., D. T. Hilleary, and B. Firdovich, 1965: A diffuse light source for calibrating meteorological satellite television cameras. Applied Optics, 4, pp. 307-309.

Joseph, J. H. and R. Davies, 1980: The albedo of cumulus cloud fields. Paper presented at International Radiation Symposium, Fort Collins, Colorado, held 11-16 August 1980.

Kattawar, G. W. and G. N. Plass, 1971: Radiance and polarization of light reflected from optically thick clouds. Appl. Opt., 10, pp. 74-80.

Klehr, J. T. and T. B. McKee, 1978: Simulated radiance patterns for MIE absorbing finite clouds. Atmospheric Science Paper #285, Colorado State University.

Kuenning, J. A., T. B. McKee, and S. K. Cox, 1978: A laboratory investigation of radiative transfer in cloud fields. Atmospheric Science Paper #286, Colorado State University.

Lenoble, J. (ed.), 1977: Standard Procedure to Compute Atmospheric Radiation Transfer in Scattering Atmosphere. International Association of Meteorology and Atmospheric Physics (IAMAP), Radiation Commission, Boulder, Colorado, July, 125 p.

McKee, T. B., J. M. Davis, S. K. Cox, 1981: Design and verification of a cloud field optical simulator. Paper presented at Fourth Conference on Atmospheric Radiation, Toronto, Canada, held 16-18 June 1981.

McKee, T. B. and S. K. Cox, 1974: Scattering of visible radiation by finite clouds. J. Atmos. Sci., 31, pp. 1885-1892.

McKee, T. B. and S. K. Cox, 1976: Simulated radiance patterns for finite cubic clouds. J. Atmos. Sci., 33, pp. 2014-2020.

McKee, T. B. and J. T. Klehr, 1978: Effects of cloud shape on scattered solar radiation. Monthly Weather Review, 106, pp. 399-404.

Ohring, G. and S. Adler, 1978: Some experiments with a zonally averaged climate model. J. Atmos. Sci., 35, pp. 186-205.

BIBLIOGRAPHIC DATA SHEET	1. Report No. CSU Report #345	2.	3. Recipient's Accession No.

4. Title and Subtitle

DIURNAL RADIANCE PATTERNS OF FINITE AND SEMI-INFINITE CLOUDS IN OBSERVATIONS OF CLOUD FIELDS

5. Report Date: December 1981

6.

7. Author(s): David M. Ebel and Thomas B. McKee

8. Performing Organization Rept. No. #345

9. Performing Organization Name and Address

Colorado State University
Atmospheric Science
Fort Collins, Colorado 80523

10. Project/Task/Work Unit No.

11. Contract/Grant No. ATM78-27556

12. Sponsoring Organization Name and Address

National Science Foundation

13. Type of Report & Period Covered

14.

15. Supplementary Notes

16. Abstracts

The effects of finite and semi-infinite cloud shape on diurnal satellite observations were investigated by simulating diurnal satellite observations of a finite cubic and semi-infinite cloud and comparing these results with actual diurnal satellite observations of cloud fields. Theoretical satellite observations were created by computing relative radiances from a theoretical model which used the Monte Carlo method to simulate the scattering of solar radiation by a finite and infinite cloud for optical depths of 73.5 and 20.0. The diurnal variations in radiance for an infinite and finite cubic cloud viewed at a zenith angle (θ) of 0° were both symmetric about local noon when the maximum radiance occurred. When viewing the same clouds from an average zenith angle ($\bar{\theta}$) of 18 to 31° (measured westward from zenith), the diurnal variation in radiance for the infinite cloud was again nearly symmetric about local noon when the maximum radiance occurred. The finite cubic cloud, however, had a skewed diurnal variation in radiance with the maximum radiance occurring at 1330 LT. This was true for both optical depths.

17. Key Words and Document Analysis. 17a. Descriptors

Clouds
Satellite
Diurnal observations
Sun/cloud/satellite geometry
Angular variation in radiance

17b. Identifiers/Open-Ended Terms

17c. COSATI Field/Group

18. Availability Statement	19. Security Class (This Report) UNCLASSIFIED	21. No. of Pages 69
	20. Security Class (This Page) UNCLASSIFIED	22. Price